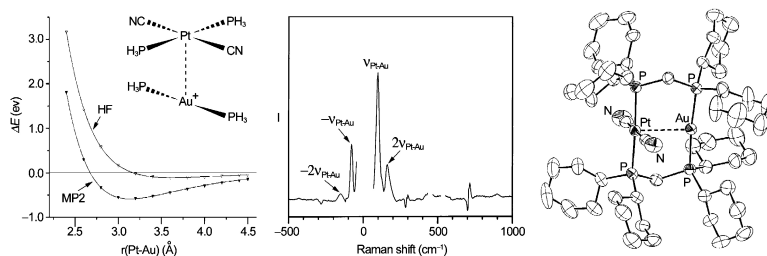Article

Metal−Metal Interactions in Heterobimetallic d−d Complexes. Structures and Spectroscopic Investigation of [M'M''(□-dcpm)(CN)] (M' = Pt, Pd; M' ' = Cu, Ag, Au) and Related Complexes by UV−vis Absorption and Resonance Raman Spectroscopy and ab Initio Calculations

Bao-Hui Xia, Hong-Xing Zhang, Chi-Ming Che, King-Hung
Leung, David Lee Phillips, Nianyong Zhu, and Zhong-Yuan Zhou

More About This Article

Additional resources and features associated with this article are available within the HTML version:

- Supporting Information
- Links to the 12 articles that cite this article, as of the time of this article download
- Access to high resolution figures
- Links to articles and content related to this article
- Copyright permission to reproduce figures and/or text from this article

View the Full Text HTML

Metal−Metal Interactions in Heterobimetallic d^8−d^{10} Complexes. Structures and Spectroscopic Investigation of [M′M″(μ-dcpm)$_2$(CN)$_2$]$^+$ (M′ = Pt, Pd; M″ = Cu, Ag, Au) and Related Complexes by UV−vis Absorption and Resonance Raman Spectroscopy and ab Initio Calculations

Bao-Hui Xia, Hong-Xing Zhang,[†] Chi-Ming Che,* King-Hung Leung, David Lee Phillips,* Nianyong Zhu, and Zhong-Yuan Zhou[‡]

Contribution from Department of Chemistry and the HKU-CAS Joint Laboratory on New Materials, The University of Hong Kong, Pokfulam Road, Hong Kong SAR, P. R. China

Received April 9, 2003; E-mail: cmche@hku.hk

Abstract: X-ray structural and spectroscopic properties of a series of heterodinuclear d^8−d^{10} metal complexes [M′M″(μ-dcpm)$_2$(CN)$_2$]$^+$ containing d^8 Pt(II), Pd(II), or Ni(II) and d^{10} Au(I), Ag(I), or Cu(I) ions with a dcpm bridging ligand have been studied (dcpm = bis(dicyclohexylphosphino)methane; M′ = Pt, M″ = Au **4**, Ag **5**, Cu, **6**; M″ = Au, M′ = Pd **7**, Ni **8**). X-ray crystal analyses showed that the metal···metal distances in these heteronuclear metal complexes are shorter than the sum of van der Waals radii of the M′ and M″ atoms. The UV−vis absorption spectra of **4**−**6** display red-shifted intense absorption bands from the absorption spectra of the mononuclear *trans*-[Pt(phosphine)$_2$(CN)$_2$] and [M″(phosphine)$_2$]$^+$ counterparts, attributable to metal−metal interactions. The resonance Raman spectra confirmed assignments of $^1[nd_\sigma^* \rightarrow (n+1)p_\sigma]$ electronic transitions to the absorption bands at 317 and 331 nm in **4** and **6**, respectively. The results of theoretical calculations at the MP2 level reveal an attractive interaction energy curve for the skewed [*trans*-Pt(PH$_3$)$_2$(CN)$_2$−Au(PH$_3$)$_2^+$] dimer. The interaction energy of Pt(II)−Au(I) was calculated to be ca. 0.45 ev.

Introduction

Over the past two decades, the spectroscopic and bonding properties of homodinuclear d^8−d^8 complexes have been extensively studied.[1] A notable example is the prototypical [Pt$_2$(P$_2$O$_5$H$_2$)$_4$]$^{4-}$, which displays an intense $5d_\sigma^* \rightarrow 6p_\sigma$ absorption band at 367 nm in its electronic absorption spectrum.[2] Such an intense absorption band being red-shifted from the absorption

spectrum of the mononuclear metal counterpart has commonly been taken as a spectroscopic signature for weak d^8−d^8 interaction in the ground state. Recently, homodinuclear d^{10}−d^{10} metal compounds with weak intramolecular metal−metal interactions have become increasingly well-recognized.[3] Metallophilicity in homodinuclear complexes of Au(I),[3e,i,j] Ag(I),[3h] and Cu(I)[3g] has been verified by various spectroscopic means and theoretical calculations.

Compared with homodinuclear metal derivatives, related studies on metal−metal interactions in heterobimetallic complexes are sparse in the literature despite the fact that there have been quite extensive reports of polynuclear heterometallic aggregates or clusters including those containing d^8 and d^{10} metal ions. Heteronuclear metal−metal bonded complexes are

† State Key Laboratory of Theoretical and Computational Chemistry, Institute of Theoretical Chemistry, Jilin University, Changchun 130023, P. R. China.

‡ Department of Applied Biology and Chemical Technology, Hong Kong Polytechnic University, Hung Hom, Kowloon, Hong Kong SAR, P. R. China.

(1) (a) Dallinger, R. F.; Miskowski, V. M.; Gray, H. B.; Woodruff, W. H. *J. Am. Chem. Soc.* **1981**, *103*, 1595−1596. (b) Rice, S. F.; Gray, H. B. *J. Am. Chem. Soc.* **1981**, *103*, 1593−1595. (c) Rice, S. F.; Milder, S. J.; Gray, H. B. *Coord. Chem. Rev.* **1982**, *43*, 349−354. (d) Stiegman, A. E.; Rice, S. F.; Gray, H. B.; Miskowski, V. M. *Inorg. Chem.* **1987**, *26*, 1112−1116. (e) Rice, S. F.; Miskowski, V. M.; Gray, H. B. *Inorg. Chem.* **1988**, *27*, 4704−4708. (f) Che, C.-M.; Yam, V. W.-W.; Wong, W.-T.; Lai, T.-F. *Inorg. Chem.* **1989**, *28*, 2908−2910. (g) Yip, H.-K.; Lai, T.-F.; Che, C.-M. *J. Chem. Soc., Dalton Trans.* **1991**, 1639−1641. (h) Bailey, J. A.; Miskowski, V. M.; Gray, H. B. *Inorg. Chem.* **1993**, *32*, 369−370. (i) Yip, H.-K.; Cheng, L.-K.; Cheung, K.-K.; Che, C.-M. *J. Chem. Soc., Dalton Trans.* **1993**, 2933−2938. (j) Navarro, J. A. R.; Romero, M. A.; Salas, J. M.; Quirós, M.; Bahraoui, J. E.; Molina, J. *Inorg. Chem.* **1996**, *35*, 7829−7835. (k) Lai, S.-W.; Chan, M. C.-W.; Cheung, T.-C.; Peng, S.-M.; Che, C.-M. *Inorg. Chem.* **1999**, *38*, 4046−4055. (l) Xia, B.-H.; Che, C.-M.; Phillips, D. L.; Leung, K.-H.; Cheung, K.-K. *Inorg. Chem.* **2002**, *41*, 3866−3875. (m) Xia, B.-H.; Che, C.-M.; Zhou, Z.-Y. *Chem.—Eur. J.* **2003**, *9*, 3055.

(2) Roundhill, D. M.; Gray, H. B.; Che, C.-M. *Acc. Chem. Res.* **1989**, *22*, 55−61.

(3) (a) Harvey, P. D.; Gray, H. B. *J. Am. Chem. Soc.* **1988**, *110*, 2145−2147. (b) Che, C.-M.; Kwong, H.-L.; Yam, V. W.-W.; Cho, K. C. *J. Chem. Soc., Chem. Commun.* **1989**, 885−886. (c) King, C.; Wang, J.-C.; Khan, M. N. I.; Fackler, J. P., Jr. *Inorg. Chem.* **1989**, *28*, 2145−2149. (d) Perreault, D.; Drouin, M.; Michel, A.; Miskowski, V. M.; Schaefer, W. P.; Harvey, P. D. *Inorg. Chem.* **1992**, *31*, 695−702. (e) Fu, W.-F.; Chan, K.-C.; Miskowski, V. M.; Che, C.-M. *Angew. Chem., Int. Ed.* **1999**, *38*, 2783−2785. (f) Leung, K.-H.; Phillips, D. L.; Tse, M.-C.; Che, C.-M.; Miskowski, V. M. *J. Am. Chem. Soc.* **1999**, *121*, 4799−4803. (g) Che, C.-M.; Mao, Z.; Miskowski, V. M.; Tse, M.-C.; Chan, C.-K.; Cheung, K.-K.; Phillips, D. L.; Leung, K.-H *Angew. Chem., Int. Ed.* **2000**, *39*, 4084−4088. (h) Che, C.-M.; Tse, M.-C.; Chan, M. C. W.; Cheung, K.-K.; Phillips, D. L.; Leung, K.-H. *J. Am. Chem. Soc.* **2000**, *122*, 2464−2468. (i) Rawashdeh-Omary, M. A.; Omary, M. A.; Patterson, H. H.; Fackler, J. P., Jr. *J. Am. Chem. Soc.* **2001**, *123*, 11237−11247. (j) Fu, W.-F.; Chan, K.-C.; Cheung, K.-K.; Che, C.-M. *Chem.—Eur. J.* **2001**, *7*, 4656−4664. (k) Zhang, H.-X.; Che, C.-M. *Chem.—Eur. J.* **2001**, *7*, 4887−4893.

of interest in different perspectives. First, mixed bi- and polymetallic complexes are known to mediate multielectron catalytic reactions. Second, the different electronegativities between metal ions lead to polarized $M^{\delta-} \rightarrow M'^{\delta+}$ bonding in the ground state, and hence, it is feasible to have $M \rightarrow M'$ charge-transfer excitation that generates a reactive zwitterionic ion in an excited state.[4] For weak metal–metal bonded complexes, Balch and co-workers first reported structural and spectroscopic studies on the d^8–d^{10} Ir[I]–Au[I] complexes such as [IrAu(μ-dppm)$_2$(CO)Cl]PF$_6$ (dppm = bis(diphenylphosphino)methane),[5a] [IrAu(μ-dppm)$_2$(CNCH$_3$)](PF$_6$)$_2$,[5b] and [IrAu(μ-dppm)$_2$(CNCH$_3$)$_3$]-(PF$_6$)$_2$.[5b] Subsequently, Che and co-workers reported the absorption and emission properties of the related [PtAu(μ-dppm)$_2$-(CN)$_2$]ClO$_4$,[6a] [PtAg(μ-dppm)$_2$(CN)(CF$_3$SO$_3$)],[6b] and [PtM-(μ-dppm)$_2$(C≡CPh)$_2$]PF$_6$ (M = Au or Ag),[6c] and tentative assignments as $nd_\sigma^* \rightarrow (n+1)p_\sigma$ transitions for these complexes were made. Vogler and co-workers[7] reported that [Pt$_2$(P$_2$O$_5$H$_2$)$_4$]$^{4-}$ in the presence of Au(CN)$_2^-$ in degassed aqueous solution exhibits a low energy luminescence band at 571 nm, which was assigned to exciplex formation resulting from direct Pt(II)–Au(I) interactions. Recently, Laguna and Pyykkö reported experimental and theoretical studies on the interactions between Pd(II) and Au(I) ions.[8] The crystal structure of [{AuCl(Ph$_2$-PCH$_2$SPh)}$_2$PdCl$_2$] showed that the sterically unhindered Pd-(II) and Au(I) centers are separated by a distance of 3.14 Å. Further calculations suggested that the Pd(II)–Au(I) interaction can mainly be attributed to a dispersion contribution.

Previously, we employed absorption and resonance Raman spectroscopies to study metal–metal interactions in dinuclear d^{10}–d^{10} [3f–h] and d^8–d^8 [9,11] metal complexes. In this work, we have prepared six heteronuclear complexes containing d^8 Pt-(II), Pd(II), and Ni(II) and d^{10} Au(I), Ag(I), and Cu(I) ions. X-ray crystal analyses have revealed close metal–metal contacts in these complexes. Electronic absorption and resonance Raman spectroscopy measurements and theoretical calculations were undertaken to elucidate the nature of metal–metal interactions in these heteronuclear d^8–d^{10} systems.

Experimental Section

General. (**Caution!** Perchlorate salts are potentially explosive and should be handled with care and in small amounts.) Solvents for photophysical studies were purified as described previously.[1k] Au(PPh$_3$)-Cl[10a] and [Ni$_2$(μ-dcpm)$_2$(CN)$_4$][11] were prepared by the literature methods. [M(dcpm)$_2$]Cl$_2$ (M = Pt, Pd; dcpm = bis(dicyclohexylphosphino)-methane) were prepared in a manner similar to that for their dppm analogues.[10b,c] ^{1}H and ^{31}P NMR spectra were measured on a Bruker

DRX-500 multinuclear FT-NMR spectrometer, with chemical shifts (δ, ppm) relative to tetramethylsilane (^{1}H NMR) and 85% H$_3$PO$_4$ (^{31}P NMR). Infrared spectra were recorded on a Bio-Rad FTS-165 spectrometer. Room temperature UV–vis spectra were obtained on a Hewlett-Packard 8453 diode array spectrophotometer; variable temperature UV–vis spectra were recorded on a Perkin-Elmer Lambda 900 spectrophotometer. Positive-ion FAB mass spectra were measured on a Finnigan MAT95 mass spectrometer. Elemental analyses were performed by the Institute of Chemistry, the Chinese Academy of Sciences. Details of resonance Raman measurements were described elsewhere.[11]

[Pt(dcpm)$_2$]Cl$_2$ (1). A CH$_2$Cl$_2$ solution (30 mL) of [Pt(NCCH$_3$)$_2$-Cl$_2$] (0.80 g, 2.3 mmol) and dcpm (1.93 g, 4.6 mmol) was stirred for 48 h. The resultant colorless solution was concentrated to 2 mL and filtered. The product was dried *in vacuo*. Yield: 2.20 g (88%). ^{1}H NMR (CD$_3$OD): δ 4.28 (t, –CH$_2$), 1.3–2.5 (m, C$_6$H$_{11}$). ^{31}P–{^{1}H} NMR (CD$_3$OD): δ –33.8 (t, $^1J_{PtP}$ = 1827 Hz). FAB MS: *m/z* 1012 ([M – 2Cl]$^+$). Anal. Calcd for C$_{50}$H$_{92}$P$_4$Cl$_2$Pt·0.5CH$_2$Cl$_2$: C, 53.89; H, 8.33. Found: C, 53.94; H 8.69.

[Pd(dcpm)$_2$]Cl$_2$ (2). A CH$_2$Cl$_2$ solution of [Pd(NCPh)$_2$Cl$_2$] (0.10 g, 0.26 mmol) and dcpm (0.22 g, 0.52 mmol) was stirred for 12 h to give a yellow solution. Removal of solvent gave the crude product, which was washed with diethyl ether and CH$_3$CN and dried *in vacuo*. Yield: 0.15 g (58%). ^{1}H NMR (CDCl$_3$): δ 4.20 (t, CH$_2$), 1.2–2.02 (m, C$_6$H$_{11}$). ^{31}P–{^{1}H} NMR (CDCl$_3$): δ –34.3 (s). FAB MS: *m/z* 922 ([M – 2Cl]$^+$). Anal. Calcd for C$_{50}$H$_{92}$P$_4$Cl$_2$Pd·CH$_3$CN: C, 60.30; H, 9.25; N, 1.35. Found: C, 60.72; H, 9.60; N, 1.54.

***trans*-[Pt(dcpm-*p*)$_2$(CN)$_2$] (3).** NaCN (0.045 g, 0.92 mmol) in CH$_3$-OH (4 mL) was added dropwise to a solution of **1** (0.42 g, 0.39 mmol) in CH$_3$OH (3 mL). The mixture was stirred for 24 h to give a white suspension. After removal of solvent, the solid was washed with water and recrystallized from CH$_2$Cl$_2$/diether ether. Yield: 0.15 g (36%). ^{1}H NMR (CDCl$_3$): δ 2.48 (s, CH$_2$), 1.19–2.18 (m, C$_6$H$_{11}$). ^{31}P–{^{1}H} NMR (CDCl$_3$): δ –8.1 (s), 20.9 (t, $^1J_{PtP}$ = 2255 Hz). IR (KBr): 2120 cm^{-1} (s, –CN). FAB MS: *m/z* 1065 (M$^+$). Anal. Calcd for C$_{52}$H$_{92}$N$_2$P$_4$Pt·CH$_2$Cl$_2$: C, 55.39; H, 8.24; N, 2.44. Found: C, 55.12; H, 8.79; N, 2.31.

[PtAu(μ-dcpm)$_2$(CN)$_2$]ClO$_4$ (4). A CH$_2$Cl$_2$ solution (10 mL) of **3** (0.15 g, 0.14 mmol) and Au(PPh$_3$)Cl (0.67 g, 0.14 mmol) was stirred for 2 h to give a colorless solution. Addition of diethyl ether to the solution resulted in precipitation of a white solid. The solid was collected by filtration and dissolved in CH$_3$OH (2 mL). Excess LiClO$_4$ was added to precipitate the product as a white solid, which was recrystallized by diffusing diethyl ether into a CH$_3$OH solution. Yield: 0.12 g (63%). ^{1}H NMR (CDCl$_3$): δ 2.90 (m, CH$_2$), 1.19–2.70 (m, C$_6$H$_{11}$). ^{31}P–{^{1}H} NMR (CDCl$_3$): δ 51.7 (s), 20.8 (t, $^1J_{PtP}$ = 2246 Hz). IR (KBr): 2123 cm^{-1} (s, –CN), 1119 (s, ClO$_4^-$), 1041 (s, ClO$_4^-$). FAB MS: *m/z* 1261 ([M – ClO$_4$]$^+$). Anal. Calcd for C$_{52}$H$_{92}$N$_2$P$_4$ClO$_4$-PtAu·CH$_3$OH: C, 45.71; H, 6.95; N, 2.01. Found: C, 45.72; H, 6.96; N, 1.64.

[PtAg(μ-dcpm)$_2$(CN)$_2$]CF$_3$SO$_3$ (5). A mixture of **3** (0.20 g, 0.19 mmol) and AgCF$_3$SO$_3$ (0.05 g, 0.19 mmol) in CH$_2$Cl$_2$ (10 mL) was stirred at room temperature for 12 h. Upon filtration and removal of solvent, a white solid was obtained. Crystals suitable for X-ray crystal analysis were obtained by slow evaporation of a CH$_3$OH/CH$_3$CN solution. Yield: 0.16 g (63%). ^{1}H NMR (CDCl$_3$): δ 2.75 (m, CH$_2$), 1.20–2.60 (m, C$_6$H$_{11}$). ^{31}P–{^{1}H} NMR (CDCl$_3$): δ 25.9 (d, *J* = 486 Hz), 25.5 (t, $^1J_{PtP}$ = 2205 Hz). IR (KBr): 2124 cm^{-1} (s, –CN). FAB MS: *m/z* 1171 ([M – CF$_3$SO$_3$]$^+$). Anal. Calcd for C$_{53}$H$_{92}$N$_2$F$_3$SO$_3$P$_4$-PtAg·2C$_2$H$_5$OC$_2$H$_5$ (a sample recrystallized from CH$_2$Cl$_2$/C$_2$H$_5$-OC$_2$H$_5$): C, 49.86; H, 7.68; N, 1.91. Found: C, 49.75; H, 7.47; N, 1.56.

[PtCu(μ-dcpm)$_2$(CN)$_2$]BF$_4$ (6). A CH$_3$CN solution (20 mL) of [Cu-(NCCH$_3$)$_4$]BF$_4$ (0.069 g, 0.22 mmol) and **3** (0.24 g, 0.22 mmol) was stirred under N$_2$ for 8 h. The resultant solution was concentrated to 2 mL, and diethyl ether was added to precipitate the product as a white

(4) Heyduk, A. F.; Nocera, D. G. *J. Am. Chem. Soc.* **2000**, *122*, 9415–9426.
(5) (a) Balch, A. L.; Catalano, V. J.; Olmstead, M. M. *Inorg. Chem.* **1990**, *29*, 585–586. (b) Balch, A. L.; Catalano, V. J. *Inorg. Chem.* **1991**, *30*, 1302–1308.
(6) (a) Yip, H.-K.; Che, C.-M.; Peng, S.-M. *J. Chem. Soc., Chem. Commun.* **1991**, 1626–1628. (b) Yip, H.-K.; Lin, H.-M.; Cheung, K.-K.; Che, C.-M.; Wang, Y. *Inorg. Chem.* **1994**, *33*, 1644–1651. (c) Yip, H.-K.; Lin, H.-M.; Wang, Y.; Che, C.-M. *J. Chem. Soc., Dalton Trans.* **1993**, 2939–2944.
(7) Pettijohn, C. N.; Jochnowitz, E. B.; Chuong, B.; Nagle, J. K.; Vogler, A. *Coord. Chem. Rev.* **1998**, *171*, 85–92.
(8) Crespo, O.; Laguna, A.; Fernández, E. J.; López-de-Luzuriaga, J. M.; Jones, P. G.; Teichert, M.; Monge, M.; Pyykkö, P.; Runeberg, N.; Schütz, M.; Werner, H. *Inorg. Chem.* **2000**, *39*, 4786–4792.
(9) Leung, K.-H.; Phillips, D. L.; Che, C.-M.; Miskowski, V. M. *J. Raman. Spectrosc.* **1999**, *30*, 987–993.
(10) (a) Bruce, M. I.; Nicholson, B. K.; Shawkataly, O. B. *Inorg. Synth.* **1989**, *26*, 324–328. (b) Cooper, G. R.; Hutton, A. T.; Langrick, C. R.; McEwan, D. M.; Pringle, P. G.; Shaw, B. L. *J. Chem. Soc., Dalton Trans.* **1984**, 855–862. (c) Hassan, F. S. M.; Markham, D. P.; Pringle, P. G.; Shaw, B. L. *J. Chem. Soc., Dalton Trans.* **1985**, 279–283.
(11) Zheng, X.; Phillips, D. L. *J. Chem. Phys.* **1998**, *108*, 5772–5783.

Scheme 1. AA′BB′ ^{31}P−{^{1}H} NMR Systems of **7** (M = Pd) and **8** (M = Ni)
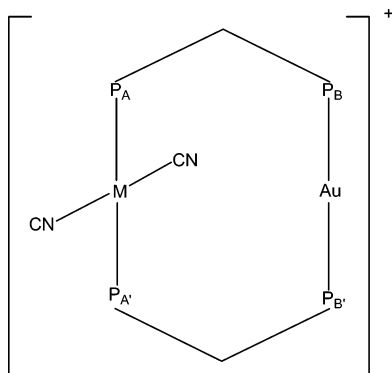
solid. Crystals suitable for X-ray crystal analysis were obtained by diffusing diethyl ether into a CH$_2$Cl$_2$ solution. Yield: 0.20 g (75%). ^{1}H NMR (CDCl$_3$): δ 2.62 (m, CH$_2$), 1.20−2.25 (m, C$_6$H$_{11}$). ^{31}P−{^{1}H} (CDCl$_3$): δ 11.4 (s), 25.6 (t, $^{1}J_{PtP}$ = 2078 Hz). ^{31}P−{^{1}H} NMR (CD$_3$-CN): δ 8.2 (s), 25.0 (t, $^{1}J_{PtP}$ = 2152 Hz). IR (KBr): 2121 cm^{-1} (s, −CN), 1124 (s, BF$_4^-$), 1084 (s, BF$_4^-$). FAB MS: *m/z* 1128 ([M − BF$_4$]$^+$). Anal. Calcd for C$_{52}$H$_{92}$N$_2$BF$_4$P$_4$PtCu·CH$_2$Cl$_2$: C, 48.98; H, 7.29; N, 2.16. Found: C, 49.42; H, 7.24; N, 1.82.

[PdAu(μ-dcpm)$_2$(CN)$_2$]Cl (7a). NaCN (0.013 g, 0.26 mmol) in CH$_3$-OH (4 mL) was added dropwise to a solution of **2** (0.10 g, 0.11 mmol) in CH$_3$OH (2 mL). After the solution was stirred for 24 h, a white suspension was obtained. The suspension was filtered to give a white solid, which was washed with water, dried, and dissolved in CH$_2$Cl$_2$ (5 mL). Au(PPh$_3$)Cl (0.55 g, 0.11 mmol) was added, and the mixture was stirred at room temperature for 10 h. A white solid precipitated upon addition of diethyl ether. Yield: 0.10 g (75%). Crystals suitable for X-ray crystal analysis were obtained by diffusing diethyl ether into a CH$_3$OH solution. ^{1}H NMR (CDCl$_3$): δ 2.93 (t, CH$_2$), 1.20−2.50 (m, C$_6$H$_{11}$). ^{31}P−{^{1}H} NMR (CDCl$_3$): δ 53.4 (t, $^{2}J(P_AP_B)$ + $^{4}J(P_AP_{B'})$ = 40 Hz), 33.9 (t, $^{2}J(P_BP_A)$ + $^{4}J(P_BP_{A'})$ = 40 Hz) (see Scheme 1). IR (KBr): 2114 cm^{-1} (s, −CN). FAB MS: *m/z* 1172 ([M − Cl]$^+$). Anal. Calcd for C$_{52}$H$_{92}$N$_2$P$_4$ClPdAu·CH$_2$Cl$_2$: C, 49.23; H, 7.33; N, 2.17. Found: C, 48.99; H, 7.45; N, 1.73.

[PdAu(μ-dcpm)$_2$(CN)$_2$]ClO$_4$ (7b). This complex was obtained as a white solid by adding excess LiClO$_4$ to a CH$_3$OH solution of **7a** followed by washing the resultant precipitate with water and diethyl ether. Yield: 80%. ^{1}H NMR (CDCl$_3$): δ 2.80 (t, CH$_2$), 1.20−2.60 (m, C$_6$H$_{11}$). ^{31}P−{^{1}H} NMR (CDCl$_3$): δ 53.4 (t, $^{2}J(P_AP_B)$ + $^{4}J(P_AP_{B'})$ = 40 Hz), 33.7(t, $^{2}J(P_BP_A)$ + $^{4}J(P_BP_{A'})$ = 40 Hz). IR (KBr): 2130 cm^{-1} (s, −CN), 1122 (s, ClO$_4^-$), 1097 (s, ClO$_4^-$). FAB MS: *m/z* 1172 ([M − ClO$_4$]$^+$). Anal. Calcd for C$_{52}$H$_{92}$N$_2$O$_4$P$_4$ClPdAu·CH$_3$OH: C, 48.81; H, 7.42; N, 2.15. Found: C, 48.42; H, 6.98; N, 2.50.

[NiAu(μ-dcpm)$_2$(CN)$_2$]ClO$_4$ (8). A mixture of [Ni$_2$(μ-dcpm)$_2$(CN)$_4$] (0.13 g, 0.12 mmol) and dcpm (0.10 g, 0.24 mmol) in CH$_2$Cl$_2$ (6 mL) was stirred for 12 h to give an orange solution. Au(PPh$_3$)Cl (0.12 g, 0.24 mmol) was added. After 24 h, the solution was evaporated to dryness, and the solid residue was dissolved in CH$_3$OH (1 mL). LiClO$_4$ was added to give the product as an orange precipitate. Crystals suitable for X-ray crystal analysis were obtained by diffusing diethyl ether into a CH$_3$OH solution. Yield: 0.02 g (7%). ^{1}H NMR (CD$_3$OD): δ 2.78 (t, CH$_2$), 1.20−2.50 (m, C$_6$H$_{11}$). ^{31}P−{^{1}H} NMR (CD$_3$OD): δ 55.7 (q, $^{2}J(P_AP_B)$ + $^{4}J(P_AP_{B'})$ = 60 Hz), 35.3(q, $^{2}J(P_BP_A)$ + $^{4}J(P_BP_{A'})$ = 58 Hz). IR (KBr): 2111 cm^{-1} (s, −CN), 1084 (s, ClO$_4^-$), 1079 (s, ClO$_4^-$). FAB MS: *m/z* 1124 ([M − ClO$_4$]$^+$). Anal. Calcd for C$_{52}$H$_{92}$N$_2$O$_4$P$_4$-ClNiAu·CH$_3$OH: C, 50.67; H, 7.70; N, 2.23. Found: C, 50.35; H, 7.20; N, 2.61.

Computational Details. (i) [PtM(μ-H$_2$PCH$_2$PH$_2$)$_2$(CN)$_2$]$^+$ (M = Au or Cu). In this work, [PtM(μ-H$_2$PCH$_2$PH$_2$)$_2$(CN)$_2$]$^+$ (M = Au or Cu) was used as the model for the corresponding [PtM(μ-dcpm)$_2$(CN)$_2$]$^+$ cation for computations. In the calculations, quasi-relativistic pseudo-

potentials of the Pt, Au, Cu, and P atoms proposed by Hay and Wadt[12] with 18, 19, 19, and 5 valence electrons and the LANL2DZ basis sets with one f-polarization function for metal and one d for P atoms (α$_f$ = 0.18 for Pt, 0.20 for Au and Cu; α$_d$ = 0.34 for P) were adopted. Thus, the basis sets were taken as Pt, Au, Cu, (8s6p4d1f)/[3s3p2d1f]; P, (3s3p1d)/[2s2p1d]; N, (10s5p)/[3s2p]; C, (10s5p)/[3s2p]; and H, (4s)/[2s].

The ground state structures were optimized at the second-order Møller−Plesset (MP2) level.[13] In the crystalline forms, complex **4** has a pseudo-C_2 symmetry with the [PtAuP$_4$] unit having a chair conformation (*vide infra*). Therefore, the model [PtAu(μ-H$_2$PCH$_2$PH$_2$)$_2$(CN)$_2$]$^+$ cation was set to have a C_2 symmetry and a chair conformation for the [PtAuP$_4$] unit. In the crystal structure of **6**, the [PtCuP$_4$] unit has a boat conformation. Thus, for the [PtCu(μ-H$_2$PCH$_2$PH$_2$)$_2$(CN)$_2$]$^+$ cation, the geometrical structure was optimized at two models: one has a C_2 symmetry with a [PtCuP$_4$] unit in chair conformation and the other has a C_s symmetry with a [PtCuP$_4$] unit in a boat conformation. For the C_2 symmetry model, the z-axis was coincident with the Pt−M vector and the y-axis was set to parallel the C−C (of −CH$_2$) vector. For the C_s symmetry one, the xz-plane is the symmetrical plane and the y-axis was set to parallel the C−C (of −CH$_2$) vector. Based on the optimized ground state structures, single excitation configuration interaction (CIS)[14] calculations on [PtAu(μ-H$_2$PCH$_2$PH$_2$)$_2$(CN)$_2$]$^+$ were performed to reveal the nature of electronic transition for the low-lying excited state. Here, we adopted the isodensity polarized continuum model (IPCM)[15] in a self-consistent reaction field (SCRF) to account for the effect of acetonitrile or dichloromethane solvent molecules on the electronic transition.

(ii) [*trans*-Pt(PH$_3$)$_2$(CN)$_2$−Au(PH$_3$)$_2^+$]. The Pt(II)−Au(I) interaction between the ground state of *trans*-[Pt(PH$_3$)$_2$(CN)$_2$] and [Au(PH$_3$)$_2$]$^+$ was calculated. In this calculation, the 18- and 19-VE (valence electron) quasi-relativistic pseudopotentials and basis sets of Andrae[16] with an additional f-polarization function (α$_f$ = 0.14 for Pt,[17] 0.2 for Au[18]) for Pt and Au atoms were used. The relatively large basis sets adopted for [*trans*-Pt(PH$_3$)$_2$(CN)$_2$−Au(PH$_3$)$_2^+$] aim at evaluating more accurately the d^8−d^{10} bonding interaction. For the P atom, the same basis set and pseudopotential as for [PtM(μ-H$_2$PCH$_2$PH$_2$)$_2$(CN)$_2$]$^+$ (M = Au or Cu) were used with an additional d-polarization function (α$_d$ = 0.334[19]). For C, N, and H atoms, the standard 6-31g* basis sets were used. The structures of *trans*-[Pt(PH$_3$)$_2$(CN)$_2$], [Au(PH$_3$)$_2$]$^+$ monomers, and the dimer [*trans*-Pt(PH$_3$)$_2$(CN)$_2$−Au(PH$_3$)$_2^+$] were partially optimized at the MP2 level. The [*trans*-Pt(PH$_3$)$_2$(CN)$_2$−Au(PH$_3$)$_2^+$] dimer was configured to have either an eclipsed or a skewed geometry (see Scheme 2a), and the P−Pt−Au and P−Au−Pt angles are not fixed at 90° but optimized. The optimized structures of *trans*-[Pt(PH$_3$)$_2$(CN)$_2$], [Au-(PH$_3$)$_2$],$^+$ and [*trans*-Pt(PH$_3$)$_2$(CN)$_2$−Au(PH$_3$)$_2^+$] were used for calculating the Pt(II)−Au(I) interaction energy by varying r(Pt−Au). The interaction energy between *trans*-[Pt(PH$_3$)$_2$(CN)$_2$] and [Au(PH$_3$)$_2$]$^+$ was obtained according to eq 1; the counterpoise (CP) corrections for basis-set superposition errors (BSSE)[20] were taken into account.

$$\Delta E_{cp} = E_{Pt-Au}^{(Pt-Au)} - E_{Pt}^{(Pt-Au)} - E_{Au}^{(Pt-Au)} = V_{int}(r) \quad (1)$$

The term ΔE_{cp} is the interaction energy with CP corrections. $E_{Pt-Au}^{(Pt-Au)}$ is the energy of the dimer [*trans*-Pt(PH$_3$)$_2$(CN)$_2$−

(12) (a) Hay, P. J.; Wadt, W. R. *J. Chem. Phys.* **1985**, *82*, 299−310. (b) Hay, P. J.; Wadt, W. R. *J. Chem. Phys.* **1985**, *82*, 284−298.
(13) Møller, C.; Plesset, M. S. *Phys. Rev.* **1934**, *46*, 618−622.
(14) Foresman, J. B.; Head-Gordon, M.; Pople, J. A.; Frisch, M. J. *J. Chem. Phys.* **1992**, *96*, 135−149.
(15) Foresman, J. B.; Keith, T. A.; Wiberg, K. B.; Snoonian, J.; Frisch, M. J. *J. Phys. Chem.* **1996**, *100*, 16098.
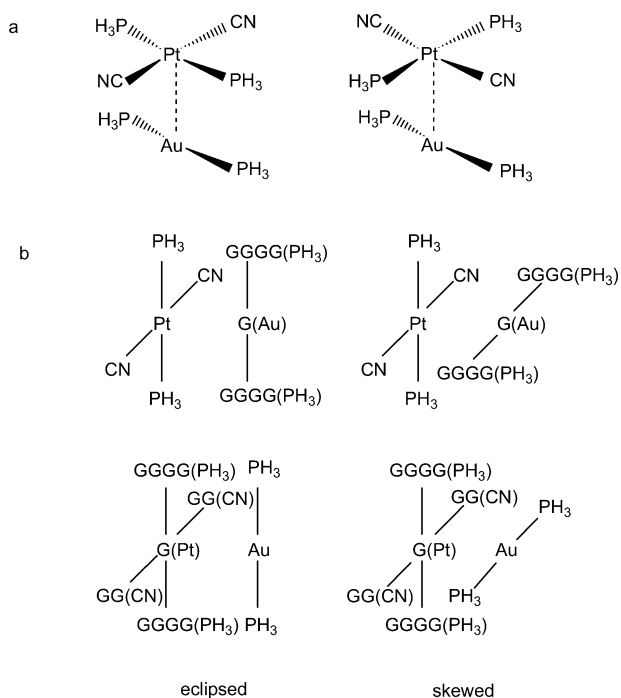(16) Andrae, D.; Haussermann, U.; Dolg, M.; Stoll, H.; Preuss, H. *Theor. Chim. Acta* **1990**, *77*, 123−141.
(17) Dolg, M.; Pyykkö, P.; Runeberg, N. *Inorg. Chem.* **1996**, *35*, 7450−7451.
(18) Pyykkö, P.; Runeberg, N.; Mendizabal, F. *Chem.—Eur. J.* **1997**, *3*, 1451−1457.
(19) Check, C. E.; Faust, T. O.; Bailey, J. M.; Wright, B. J.; Gilbert, T. M.; Sunderlin, L. S. *J. Phys. Chem. A* **2001**, *105*, 8111−8116.
(20) Boys, S. F.; Bernardi, F. *Mol. Phys.* **1970**, *19*, 553.

Scheme 2[a]

eclipsed   skewed

[a] (a) Orientations of eclipsed and skewed [*trans*-Pt(PH$_3$)$_2$(CN)$_2$–Au(PH$_3$)$_2$$^+$] dimer and (b) schematic structures for calculating interaction energy curve with CP (counterpoise) correction. "G" denotes the atoms that were treated as "ghost" atoms; that is, the Gaussian basis functions at the corresponding position were taken into account but the charge was zero. The upper layer is for *trans*-[Pt(PH$_3$)$_2$(CN)$_2$], and the lower layer is for [Au(PH$_3$)$_2$]$^+$. The dimer energy was calculated on the structure shown in part a.

Au(PH$_3$)$_2$$^+$], which was calculated based on the optimized geometry except varying r(Pt–Au). $E_{Pt}^{(Pt–Au)}$ and $E_{Au}^{(Pt–Au)}$ are the respective energies of *trans*-[Pt(PH$_3$)$_2$(CN)$_2$] and [Au(PH$_3$)$_2$]$^+$ at r(Pt–Au) value with the CP correction[20] (see Scheme 2b).

An alternative partitioning of the interaction energies depicted in eq 1 is given in eq 2, where ΔE(HF) is the interaction energy evaluated from self-consistent field (SCF) calculations at the Hartree–Fork (HF) level; $\Delta E^{(2)}$ is the second-order correlation interaction energy.

$$\Delta E(\text{MP2}) = \Delta E(\text{HF}) + \Delta E^{(2)} = V_{int}(r) \qquad (2)$$

Usually, the intermolecular potential V_{int} can be partitioned into four contributions (eq 3):

$$V_{int} = V_{short} + V_{elect} + V_{ind} + V_{disp} \qquad (3)$$

The four terms are the short-range, electrostatic, induction, and dispersion contributions, respectively.[21] It is common practice to associate the Hartree–Fork term (ΔE(HF)) with the sum of V_{short}, V_{elect}, and V_{ind}, while the $\Delta E^{(2)}$ (see eq 2) electron correlation term is associated with dispersion (V_{disp}).[21]

We fitted the calculated interaction energy points using the Morse type potential, as described by eq 4.[22]

$$\Delta E(r) = D\{[1 - \exp(-a[r - r_0])]^2 - 1\} \qquad (4)$$

All calculations were performed using the GAUSSIAN 98 program package.[23]

(21) Buckingham, A. D.; Fowler, P. W.; Hutson, J. M. *Chem. Rev.* **1988**, *88*, 963–988.
(22) Spuhler, P.; Holthausen, M. C.; Nachtigallová, D.; Nachtigall, P.; Sauer, J. *Chem.—Eur. J.* **2002**, *8*, 2099–2115.

X-ray Crystallography. Crystal data and details of collection and refinement are listed in Table S1 (see Supporting Information). Graphite monochromatized Mo Kα radiation ($\lambda = 0.710\ 73$ Å) was used, and all the non-hydrogen atoms were refined anisotropically. All the hydrogen atoms were placed at calculated positions without refinement.

The crystal data were collected at 301 K (**4**·2CH$_3$OH and **8**·2CH$_3$-OH) or 253 K (**7a**·0.5C$_2$H$_5$OC$_2$H$_5$·1.5H$_2$O) on an MAR diffractometer with a 300 mm image plate detector. The images were interpreted and intensities integrated using program DENZO.[24] The structures were solved by direct method (SIR92[25a] for **4**·2CH$_3$OH and SIR97[25b] for **7a**·0.5C$_2$H$_5$OC$_2$H$_5$·1.5H$_2$O and **8**·2CH$_3$OH) and refined by full-matrix least-squares using the software package TeXsan[26] (**4**·2CH$_3$OH) or SHELXL-97 program[27] (**7a**·0.5C$_2$H$_5$OC$_2$H$_5$·1.5H$_2$O and **8**·2CH$_3$OH) on a Silicon Graphics Indy computer. For **4**·2CH$_3$OH, two O atoms of ClO$_4$$^-$ were disordered with O(3), O(3′), O(4), and O(4′) having occupation numbers of 0.65, 0.35, 0.7, and 0.3, respectively. In the least-squares refinement, the disordered O atoms were refined isotropically.

For **5**·CH$_3$OH and **6**·CH$_2$Cl$_2$, the diffraction data were collected at 294 K on a Bruker SMART CCD diffractometer. The structures were solved by direct method and refined by full-matrix least-squares against F^2 using the SHELXL-97 program[27] on a PC.

Results

Syntheses and Characterization. Shaw and co-workers[10b,c] first reported the syntheses and characterization of heterobimetallic d⁸−d¹⁰ metal complexes containing Pt(II) and Au(I)/Ag-(I)/Cu(I) ions with the dppm bridging ligands; they also reported related acetylide complexes of Pd(II)−Ag(I)[28] and Ni(II)−Au-(I)[29] bridged by dppm ligands. In this work, we have employed dcpm instead of dppm to give dinuclear metal complexes. The dcpm ligand was chosen because it is optically transparent in the UV−vis region and allows unambiguous identification of nd$_\sigma$*→(n + 1)p$_\sigma$ transition.

We prepared *trans*-[M(dcpm-p)$_2$(CN)$_2$] (M = Pt or Pd) by a method similar to that for *trans*-[M(dppm-p)$_2$(CN)$_2$].[10c] Complex *trans*-[Pt(dcpm-p)$_2$(CN)$_2$] (**3**) was characterized by NMR spectroscopy and FAB mass spectrometry. Shaw[10c] and co-workers reported that the ^{31}P−{^{1}H} NMR spectrum of *trans*-[Pt(dppm-p)$_2$(CN)$_2$] shows fluxional behavior, featuring two broad ^{31}P signals at room temperature with the ^{31}P satellites arising from

(23) Frisch, M. J.; Trucks, G. W.; Schlegel, H. B.; Scuseria, G. E.; Robb, M. A.; Cheeseman, J. R.; Zakrzewski, V. G.; Montgomery, J. A., Jr.; Stratmann, R. E.; Burant, J. C.; Dapprich, S.; Millam, J. M.; Daniels, A. D.; Kudin, K. N.; Strain, M. C.; Farkas, O.; Tomasi, J.; Barone, V.; Cossi, M.; Cammi, R.; Mennucci, B.; Pomelli, C.; Adamo, C.; Clifford, S.; Ochterski, J.; Petersson, G. A.; Ayala, P. Y.; Cui, Q.; Morokuma, K.; Rega, N.; Salvador, P.; Dannenberg, J. J.; Malick, D. K.; Rabuck, A. D.; Raghavachari, K.; Foresman, J. B.; Cioslowski, J.; Ortiz, J. V.; Baboul, A. G.; Stefanov, B. B.; Liu, G.; Liashenko, A.; Piskorz, P.; Komaromi, I.; Gomperts, R.; Martin, R. L.; Fox, D. J.; Keith, T.; Al-Laham, M. A.; Peng, C. Y.; Nanayakkara, A.; Challacombe, M.; Gill, P. M. W.; Johnson, B.; Chen, W.; Wong, M. W.; Andres, J. L.; Gonzalez, C.; Head-Gordon, M.; Replogle, E. S.; Pople, J. A. *Gaussian 98*, revision A.11.3; Gaussian, Inc.: Pittsburgh, PA, 2002
(24) Gewrith, D. (written by with the cooperation of the program authors Otwinowski, Z. and Minor, W.) In *The HKL Manual − A description of programs DENZO, XDISPLAY, and SCALEPACK*; Yale University: New Haven, CT, 1995.
(25) (a) For SIR92, see: Altomare, A.; Cascarano, M.; Giacovazzo, C.; Guagliardi, A.; Burla, M. C.; Polidori, G.; Camalli, M. *J. Appl. Cryst.* **1994**, *27*, 435. (b) For SIR97, see: Altomare, A.; Burla, M. C.; Camalli, M.; Cascarano, G.; Giacovazzo, C.; Guagliardi, A.; Moliterni, A. G. G.; Polidori, G.; Spagna, R. *J. Appl. Cryst.* **1998**, *32*, 115−119.
(26) *TeXsan: Crystal Structure Analysis Package*; Molecular Structure Corporation: The Woodlands, Texas, 1985 and 1992.
(27) For SHELX-97, see: Sheldrick, G. M. 1997. *SHELX-97 Programs for Crystal Structure Analysis*, release 97−2; University of Göttingen: Göttingen, Germany.
(28) Langrick, C. R.; Pringle, P. G.; Shaw, B. L. *Inorg. Chim. Acta* **1983**, *76*, L263−L264.
(29) Fontaine, X. L. R.; Higgins, S. J.; Langrick, C. R.; Shaw, B. L. *J. Chem. Soc., Dalton Trans.* **1987**, 777−779.

coupling to the ^{195}Pt nuclei being not well resolved. In this work, the ^{31}P–{^{1}H} NMR spectrum of **3** shows two sets of well resolved signals at room temperature: one is a triplet centered at δ 20.9 attributable to the P atom ligated to Pt(II) with a ^{31}P–^{195}Pt coupling constant of 2255 Hz; the other is a singlet corresponding to the uncoordinated P atom. The ^{31}P–{^{1}H} NMR data confirm the trans and monohapto structure of **3**. Attempts to isolate the Pd(II) and Ni(II) analogues of **3**, that is, *trans*-[Pd(dcpm-*p*)$_2$(CN)$_2$] and *trans*-[Ni(dcpm-*p*)$_2$(CN)$_2$], as a pure product by a method similar to that for **3** were not successful. We were also not able to obtain the mononuclear [Ni(dcpm)$_2$]$^{2+}$ complex.

Three heteronuclear complexes **4**–**6** were obtained by reacting **3** with Au(PPh$_3$)Cl, AgCF$_3$SO$_3$, and [Cu(NCCH$_3$)$_4$]BF$_4$, respectively. The ^{31}P–{^{1}H} NMR spectra of these three complexes display two sets of signals consistent with their chemical formulations. The ^{31}P–{^{1}H} NMR spectrum of **5** at room temperature shows a 1:1 doublet centered at $\delta = 25.9$ with $J = 486$ Hz attributable to ^{31}P–$^{107/109}$Ag (the ^{31}P–^{107}Ag and ^{31}P–^{109}Ag couplings were not resolved under the NMR conditions) and a triplet at $\delta = 25.5$ with $J = 2205$ Hz attributable to ^{31}P–^{195}Pt coupling. The ^{31}P–{^{1}H} NMR spectra of **6** in CDCl$_3$ and CD$_3$CN solutions are slightly different in that the signal corresponding to the P atoms ligated to Cu(I) in CD$_3$CN is shifted upfield by ~3 ppm compared to that recorded in CDCl$_3$ solution. This is indicative of the different coordination environment around the Cu atom in these two solvent systems.

The ^{31}P–{^{1}H} NMR spectra of **7a,b** are essentially identical, suggesting that the counteranion has insignificant effect on the structure of the [PdAu(μ-dcpm)$_2$(CN)$_2$]$^+$ cation in solution. The ^{31}P–{^{1}H} NMR spectra of **7a,b** and **8** are consistent with AA′BB′ spin systems (Scheme 1), as previously found in other heterometallic complexes containing palladium[28] and nickel.[29] Complex **8** is one of the rare examples of dinuclear Ni(II)–Au(I) complexes that have been identified.

X-ray Crystal Structures. The X-ray crystal structures of **4**–**8** are similar except for the [M′M″P$_4$] macrocycle, which is in chair conformation in **4**, **5**, **7a**, and **8** and boat conformation in **6**. The perspective drawing of **4** is shown in Figure 1 and those for the others are given in the Supporting Information (Figures S1–S4). Selected bond distances and angles are also given in the Supporting Information (see Table S2). In **4**–**6**, the Pt atoms exhibit a distorted square planar geometry with the P–Pt–P angles ranging from 174.51(3)°–177.68(4)°. The P–Au–P and P–Ag–P angle in **4** and **5** are 174.21(5)° and 173.64(5)°, respectively. In contrast, the P–Cu–P angle of 166.34(3)° in **6** substantially deviates from 180.0° for a linear geometry, indicating significant distortion of the P–Cu–P axis from linearity. In **4**, the Au–Pt–C angles are close to 90°; this is different from [PtAu(μ-dppm)$_2$(CN)$_2$]ClO$_4$,[6a] in which the Au–Pt–C angle is 67.1(8)°. In **5**, the counteranion CF$_3$SO$_3^-$ is uncoordinated, and this is different from its dppm analogue [PtAg(μ-dppm)$_2$(CN)$_2$(CF$_3$SO$_3$)],[6b] in which the CF$_3$SO$_3^-$ ion is weakly coordinated to the Ag atom. We attribute the structural differences between **4/5** and their dppm analogues to the larger steric effect of the dcpm ligand. In **6**, the Cu–Pt–C51 angle of 79.5(1)° substantially deviates from 90.0° and the Cu···C51 distance is 3.062 Å, so presumably there is a weak intramolecular Cu···CN interaction. However, no solvent molecule or
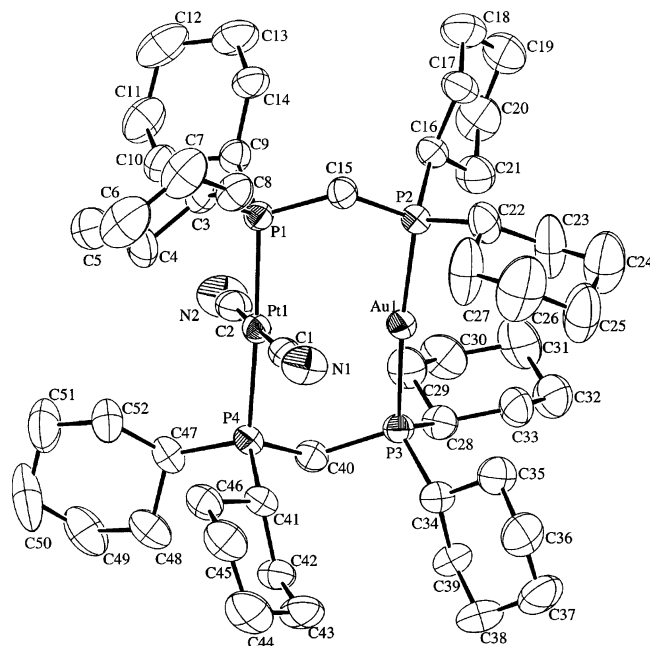

Figure 1. Perspective drawing of [PtAu(μ-dcpm)$_2$(CN)$_2$]ClO$_4$ (**4**) (H-atoms and ClO$_4^-$ are not shown).

counteranion was found to interact with Cu(I), in contrast to the [Cu$_2$(μ-dcpm)$_2$]$^{2+}$ salts where weak cation–anion interaction was found in the crystal lattice.[3g] We suggest that the intramolecular Cu···CN interaction would render the Cu(I) in **6** less accessible for Cu(I)–solvent/anion interaction. The intramolecular Pt(II)···M(I) distances in **4**, **5**, and **6** are 2.9534(4), 2.9117(6), and 2.7368(4) Å, respectively, which are shorter than the sums of the corresponding van der Waals radii[30] (3.41 Å for "Pt + Au", 3.47 Å for "Pt + Ag", and 3.15 Å for "Pt + Cu") and fall in the range expected for a weak d^8–d^{10} metal–metal interaction.

In **7a** and **8**, both the Pd and Ni atoms exhibit distorted square planar geometry with C–Pd–P or C–Ni–P angles of ca. 85–94°. The Au atom is coordinated to the two P atoms of the bridging diphosphine ligands to give a slightly distorted linear geometry, with P–Au–P angles of 172.8(1)° and 174.89(5)°. The Pd–P and Ni–P distances in **7a** and **8**, respectively, are comparable to related values found in [Pd$_2$(μ-dcpm)$_2$(CN)$_4$][1m] and [Ni$_2$(μ-dcpm)$_2$(CN)$_4$].[11] The intramolecular Pd···Au and Ni···Au distances of 2.954(1) Å and 2.8614(8) Å in **7a** and **8**, respectively, are shorter than the sums of van der Waals radii[30] of "Pd + Au" and "Ni + Au" (3.29 Å in both cases).

Electronic Spectra. The UV–vis absorption spectra of **3**–**6** at 298 K are depicted in Figure 2; those of **7a,b** and **8** at the same temperature are shown in Figure 3. Figure 4 shows the absorption spectra of **7a** at different temperatures. The spectral data for **3**–**8**, with ϵ in dm^3 mol^{-1} cm^{-1}, are summarized in Table 1.

The absorption spectrum of **3** in CH$_2$Cl$_2$ solution is featureless; there are intense absorptions with several peak maxima at 240–300 nm (ϵ (2–9) × 10^3), presumably due to overlapping dipole-allowed transitions. The absorption spectra of **4**–**6** are similar: a set of poorly resolved bands at 220–300 nm with $\epsilon < 9 \times 10^3$ and a distinct intense band at 300–330 nm with $\epsilon \approx (1.0–2.4) \times 10^4$. A very weak band at ca. 363 nm ($\epsilon \approx$

(30) Bondi, A. *J. Phys. Chem.* **1964**, *68*, 441–451.

Table 1. UV−vis Absorption and Photophysical Data (*T* = 298 K unless Otherwise Indicated)

complex	medium	λ_{abs}/nm (ϵ/dm³ mol⁻¹ cm⁻¹)	λ_{em}/nm (τ/μs)[a]	$10^3 \times \phi_{em}$[b]
trans-[Pt(dcpm-*p*)₂(CN)₂] (**3**)	CH₂Cl₂	248 (8500), 259 *sh* (7000), 273 *sh* (3400), 285 (1950)		
[PtAu(*μ*-dcpm)₂(CN)₂]ClO₄ (**4**)	CH₂Cl₂	252 (6920), 265 (6620), 317 (22200), 363 (390)	445 (0.65)	4
	CH₃CN	245 (6370), 259 (7200), 279 (4320), 316 (23200), 363 (320)	448 (0.76)	6
	CH₃OH	246 (6500), 261 (7490), 316 (22850), 363 (320)	452 (0.86)	12
	glass[c] (77 K)		433 (4.3)	
	solid		451 (0.9)	
	solid (77 K)		444 (4.0)	
[PtAg(*μ*-dcpm)₂(CN)₂]CF₃SO₃ (**5**)	CH₂Cl₂	239 (8120), 250 (8150), 279 (4073), 306 (16940)	nonemissive	
	CH₃OH	238 (8570), 256 (8480), 276 (4220), 307 (19000)	nonemissive	
	CH₃CN	237 (7920), 251 (7720), 279 (3980), 306 (17470)	nonemissive	
	glass[c] (77 K)		423 (6.7)	
	solid		450 (2.0)	
	solid (77 K)		435 (5.1)	
[PtCu(*μ*-dcpm)₂(CN)₂]BF₄ (**6**)	CH₂Cl₂	247 (8430), 271 (8810), 335 (13900)	445 *sh*, 555[d]	12
	CH₃OH	268 (7970), 331 (16380)	430 *sh* (0.5), 582 (0.8)	0.3
	CH₃CN	266 (4180), 296 (2900), 331 (9650)	457 (0.7), 575 (0.9)	0.7
	glass[c] (77 K)		445 (11), 493 (16)	
	solid		508 (6)	
[PdAu(*μ*-dcpm)₂(CN)₂]Cl (**7a**)	CH₂Cl₂	246 (21960), 265 (18100), 280 (17460), 314 (6390)	nonemissive	
	CH₃CN	246 (20430), 265 (17890), 277 (17780), 314 (5840)	516 (13)	1.8
	CH₃OH	247 (21670), 276 (21400), 314 (7040)	516 (14)	1.9
	glass[c] (77 K)		509 (45)	
	solid		519 (18)	
[PdAu(*μ*-dcpm)₂(CN)₂]ClO₄ (**7b**)	CH₃OH	247 (20840), 276 (20680), 314 (6770)		
[NiAu(*μ*-dcpm)₂(CN)₂]ClO₄ (**8**)	CH₃OH	250 (10480), 277 (26500), 305 (4500), 350 (5410), 402 (3270)	nonemissive	
	CH₂Cl₂	277 (26500), 305 (4270), 350 (5100), 400 (3070)	nonemissive	
[Au(PEt₃)₂]PF₆[e]	CH₃CN	205 (15500), 209 (14000), 238 (1740), 251 (1150)		
[Cu(PCy₃)₂]ClO₄[f]	CH₃CN	210 (23400), 230 *sh* (12500), 272 (900)		
	CH₂Cl₂	238 (11500), 248 (9700), 275 (270)		
trans-[Pd(P(*n*-Bu)₃)₂(CN)₂][g]	CH₃CN	200 (25500), 221 (22200), 228 (24800), 244 (22700)		
[Pd(DEPE)₂](PF₆)₂[g]	CH₃CN	211 (29500), 221 (29000), 242 (31000), 253 (24000)		

[a] Excitation wavelength for emission spectra measurements: 317 nm for **4**, 306 nm for **5**, 330 nm for **6**, and 310 nm for **7**. For luminescence lifetime measurements, excitation was at 355 nm. [b] The emission quantum yield was calculated with the reference of Ru(bpy)₃Cl₂·6H₂O in CH₃CN. [c] Solvent: CH₃OH/EtOH (v/v 4:1). [d] Biexponential decay (τ_1: 1.08 μs. τ_2: 5.38 μs). [e] From ref 35. [f] From ref 3g. [g] From ref 34.

3×10^2) was found for **4**. The solvent effect on the absorption spectra of **4** and **5** is negligible. For **6**, the absorption spectra in different solvents vary: the intense band at 335 nm in CH₂Cl₂ is blue-shifted to 331 nm in CH₃CN and CH₃OH, with the ϵ_{max} value in CH₃CN significantly decreased (see the inset to Figure 2).

The absorption spectrum of **7a** is solvent- and temperature-dependent. There are overlapping bands at $\lambda < 300$ nm with $\epsilon \approx (1.7-2.2) \times 10^4$ and a broad shoulder band at 310−320 nm with $\epsilon = 5000-9000$. The band at 276 nm (ϵ 24 100) in CH₃OH solution becomes resolved into two peaks with λ_{max} at 265 ($\epsilon \approx 18\,000$) and ~280 nm ($\epsilon \approx 17\,500$) in CH₂Cl₂ and CH₃CN solution. In addition, as depicted in Figure 4, decreasing the temperature from 298 to 203 K affects the UV−vis absorption spectrum of **7a** in CH₃OH. First, the broad band with λ_{max} at 276 nm splits into two bands, namely, a distinct peak at ~264 nm and a shoulder band at ~280 nm. The broad shoulder band tailing to 500 nm at 298 K becomes a distinct intense band at 203 K with a peak maximum at 303 nm. For **7b**, its

absorption spectrum in CH₃OH is the same as that of **7a**, revealing that the halide anion in the latter does not affect the electronic transitions.

The absorption spectrum of **8** in CH₃OH exhibits an intense absorption at 277 nm (ϵ 26 500), a shoulder band at 305 nm (ϵ 4500), and two lower energy absorption bands at 350 (ϵ 5410) and 402 (ϵ 3270) (see Figure 3), which are responsible for the orange color of the compound.

Emission Spectra. Photoluminescence has been detected for the heterodinuclear metal complexes. The emission and corresponding excitation spectra measured in CH₃OH/EtOH (4:1, v/v) glassy solutions at 77 K are depicted in Figures 5−7 for **4**, **6**, and **7** and in Figure S5 of the Supporting Information for **5**. The photophysical data are listed in Table 1.

Complex **4** emits in solution, the solid state, and 77 K CH₃OH/EtOH (4:1) glassy solution with an emission maximum at 433−452 nm (see Figure 5), while **5** and **7a** in solid state (298/77 K) and CH₃OH/EtOH (4:1) glassy solution (77 K) exhibit emissions at 420−450 nm (**5**, see Figure S5) and 510−520 nm
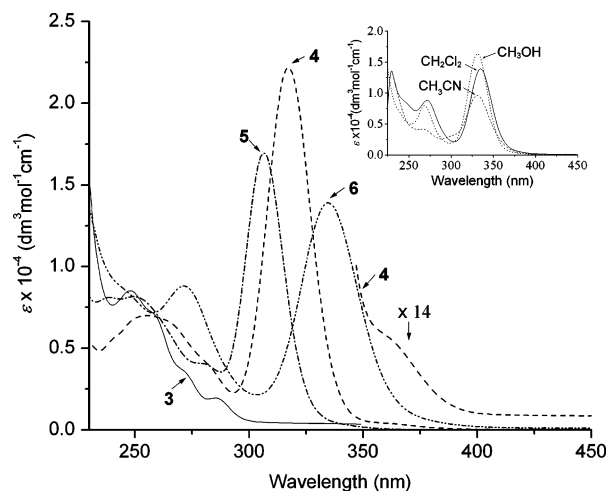
Figure 2. UV−vis absorption spectra of *trans*-[Pt(dcpm-*p*)$_2$(CN)$_2$] (**3**), [PtAu(μ-dcpm)$_2$(CN)$_2$]ClO$_4$ (**4**), [PtAg(μ-dcpm)$_2$(CN)$_2$]CF$_3$SO$_3$ (**5**), and [PtCu(μ-dcpm)$_2$(CN)$_2$]BF$_4$ (**6**) in CH$_2$Cl$_2$ at 298 K. The inset is the absorption spectra of **6** in CH$_2$Cl$_2$, CH$_3$OH, and CH$_3$CN.
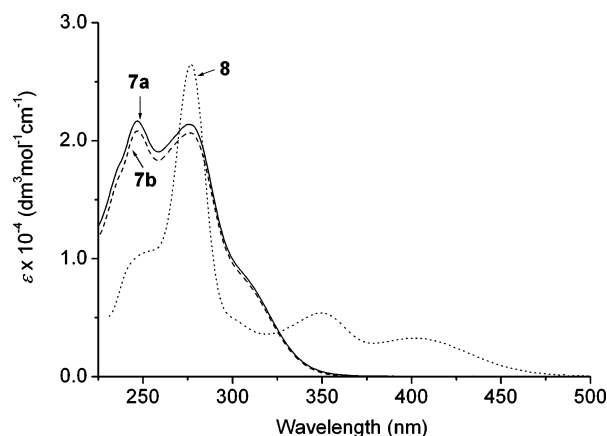
Figure 3. UV−vis absorption spectra of [PdAu(μ-dcpm)$_2$(CN)$_2$]Cl (**7a**), [PdAu(μ-dcpm)$_2$(CN)$_2$]ClO$_4$ (**7b**), and [NiAu(μ-dcpm)$_2$(CN)$_2$]ClO$_4$ (**8**) in CH$_3$OH at 298 K.
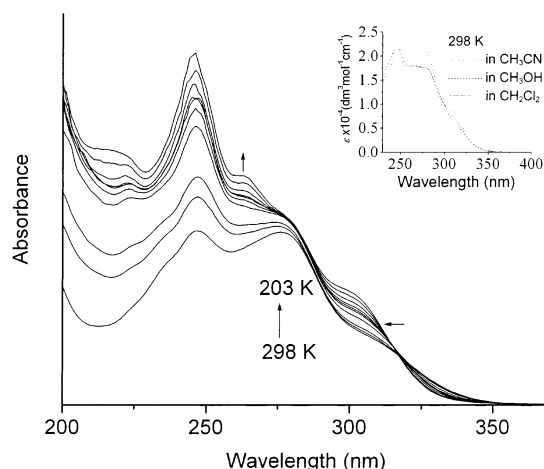

Figure 4. Absorption spectra of [PdAu(μ-dcpm)$_2$(CN)$_2$]Cl (**7a**) in CH$_3$-OH at 298−203 K. The inset is the absorption spectra of **7a** in CH$_2$Cl$_2$, CH$_3$OH, and CH$_3$CN at 298 K.

(**7a**, see Figure 7). These emissions have lifetimes in the microsecond regime. For **4** and **5**, the excitation spectra measured in 77 K glassy solutions match the corresponding absorption spectra at 298 K. However, the excitation spectrum of **7a** in 77 K glassy solution is different from the absorption
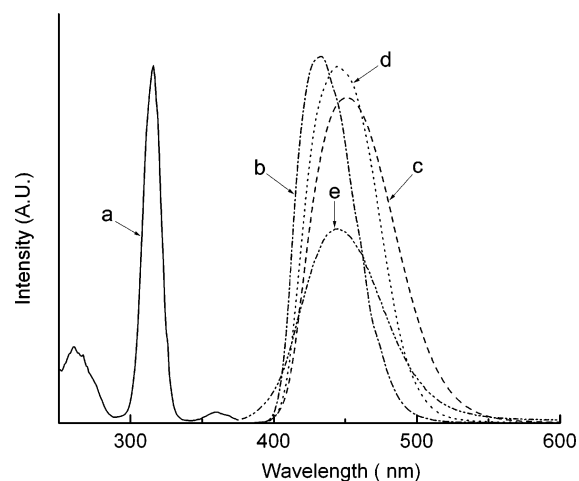

Figure 5. (a) Excitation and (b−e) emission spectra of [PtAu(μ-dcpm)$_2$-(CN)$_2$]ClO$_4$ (**4**). Measurement conditions: (a and b) in 77 K glassy solution (CH$_3$OH/EtOH 4:1), (c) in solid state at 298 K, (d) in solid state at 77 K, and (e) in CH$_2$Cl$_2$ at 298 K.
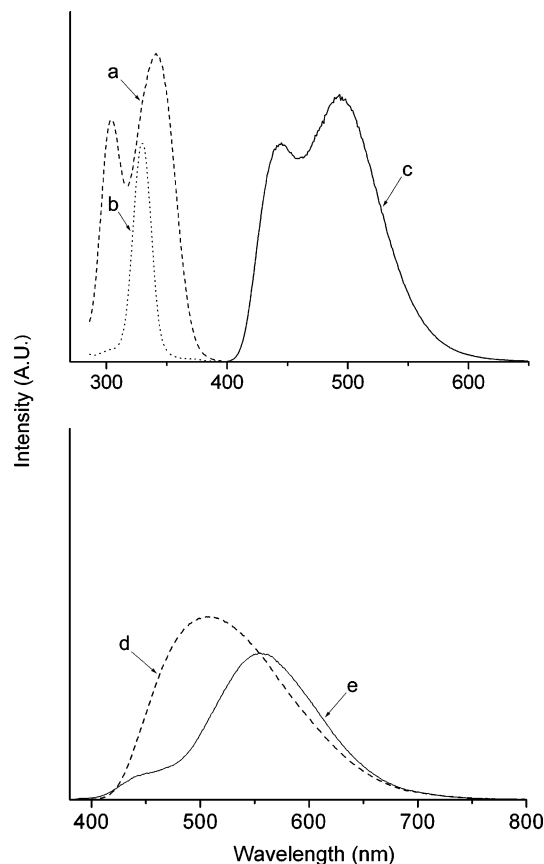

Figure 6. (a,b) Excitation spectra and (c−e) emission spectra of [PtCu-(μ-dcpm)$_2$(CN)$_2$]BF$_4$ (**6**). Measurement conditions: (a and b) monitored at 493 and 445 nm, respectively, in glassy solution (CH$_3$OH/EtOH 4:1) at 77 K, (c) in glassy solution (CH$_3$OH/EtOH 4:1) at 77 K, (d) in solid state at 298 K, and (e) in CH$_2$Cl$_2$ at 298 K.

spectrum measured at room temperature in that a distinct absorption band with a peak maximum at 299 nm is observed in the former.

The emission spectrum of **6** in the solid state at 298 K shows a broad emission band at 508 nm (Figure 6). In 77 K glassy solution (CH$_3$OH/EtOH 4:1), **6** displays two emission bands centered at 445 and 493 nm; the excitation spectra monitored at these two emission maxima are different. The excitation
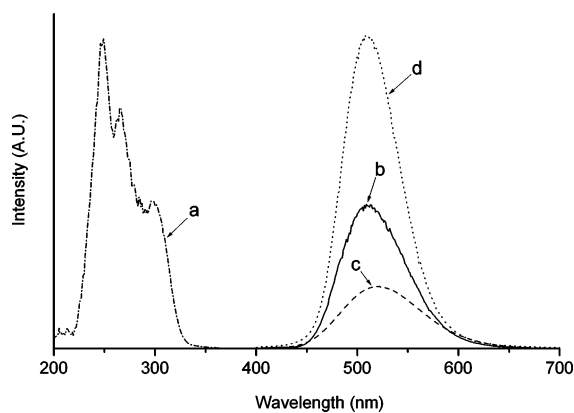
Figure 7. (a) Excitation and (b–d) emission spectra of [PdAu(μ-dcpm)$_2$-(CN)$_2$]Cl (**7a**). Measurement conditions: (a and b) in 77 K glassy solution (CH$_3$OH/EtOH 4:1), (c) in solid state at 298 K, and (d) in solid state at 77 K.

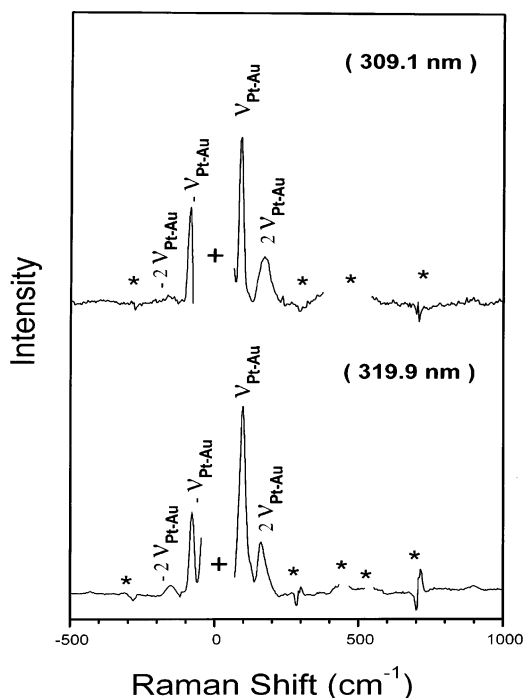**Figure 8.** Resonance Raman spectra of [PtAu(μ-dcpm)$_2$(CN)$_2$]ClO$_4$ (**4**) in CH$_2$Cl$_2$ obtained with excitation wavelengths of 309.1/319.9 nm. The spectra have been intensity corrected, and the Rayleigh line, glass bands (+ mark), and solvent bands (* mark) have been subtracted.

spectrum monitored at 445 nm emission resembles the UV–vis spectrum at 298 K, while the excitation spectrum monitored at 493 nm shows two peak maxima at 304 and 341 nm. In CH$_2$Cl$_2$, CH$_3$OH, or CH$_3$CN solution, **6** shows two emission bands: a higher-energy band centered at ca. 430–460 nm and a lower-energy band centered at ca. 550–590 nm. The emissions measured in CH$_3$OH and CH$_3$CN are weak (quantum yield $< 1 \times 10^{-3}$). All the emissions have lifetimes in the microsecond regime.

No photoluminescence was found for **8** even at 77 K.

Resonance Raman Spectra. To further probe the metal–metal interactions of the heteronuclear metal complexes, resonance Raman spectra of **4** and **6** have been recorded upon excitation into their lowest energy dipole-allowed absorption band(s). Figure 8 and Figure S6 (the latter is in the Supporting Information) show the resonance Raman spectra obtained in

Table 2. Optimized Molecular Structural Data of [PtM(μ-H$_2$PCH$_2$PH$_2$)$_2$(CN)$_2$]$^+$ (M = Au, Cu)

	M = Au		M = Cu		
	calcd	exptl (**4**)	calcd (boat)	calcd (chair)	exptl (**6**)
Bond Length (Å)					
Pt···M	2.912	2.9534(4)	2.703	2.620	2.7368(4)
Pt–P	2.321	2.333(2)	2.333	2.332	2.3307(9)
M–P	2.368	2.311(2)	2.282	2.286	2.2132(9)
Pt–C	2.017	2.009(7)	2.034/2.007	2.018	1.967(4)
C–N	1.221	1.126(7)	1.220/1.226	1.221	1.160(5)
(Pt)P–H	1.417	1.427	1.417	1.418	1.422
(M)P–H	1.418		1.419	1.419	
C–H	1.106	1.106	1.106	1.106	1.094
M–C(N)	2.017		2.293/4.127	3.237	
Bond Angle (deg)					
P–Pt–M	89.8	91.27(4)	89.9	89.6	92.67(2)
P–M–Pt	92.6	92.88(2)	99.5	100.2	96.58(2)
C–Pt–M	87.6	88.4(2)	121.7/55.8	87.5	79.5/92.9
P–Pt–P	179.7	177.04(5)	176.8	179.2	174.51(3)
P–M–P	174.9	174.21(5)	154.1	159.6	166.34(3)
C–Pt–C	175.2	176.5(3)	177.5	175.1	172.4(1)
Dihedral Angle (deg)					
P–Pt–M–P	16.2	8.5	7.1	13.7	1.8

CH$_2$Cl$_2$ solution with excitation wavelengths of 309.1/319.9 nm for **4** and 319.9/341.5/354.7 nm for **6** after intensity corrections and subtractions of the Rayleigh line, glass bands, and solvent bands. Tables S3 and S4 (see Supporting Information) give the wavenumbers, relative resonance Raman intensities and absolute resonance Raman cross-section values for **4** and **6**, respectively. The Raman intensity appears in a single low-frequency mode and its overtones. The fundamental frequency and overtones are found to be 85/170 cm^{-1} for **4** and 117/234 cm^{-1} for **6**.

Computational Results. The optimized structural data of [PtM(μ-H$_2$PCH$_2$PH$_2$)$_2$(CN)$_2$]$^+$ (M = Au, Cu) are summarized in Table 2. The calculated Pt···Au distance of 2.912 Å and other main structural parameters for the [PtAu]$^+$ model are consistent with the X-ray crystallographic data of **4** except for the P–Pt–Au–P dihedral angle of 16.2°, which deviates from the X-ray crystallographic data of 8.5°. We suggest this discrepancy arises from the fact that the X-ray data was obtained with the complex in a rigid crystal lattice but calculation of the model compound was performed with a floppy gas-phase model. The calculated Pt···Cu distance of 2.703 Å for the boat conformation of [PtCu-(μ-H$_2$PCH$_2$PH$_2$)$_2$(CN)$_2$]$^+$ is close to the X-ray crystallographic result of 2.7368(4) Å in **6**, but for the chair conformation, the calculated Pt···Cu distance is 0.11 Å shorter. Another point of note is that the optimization gives a shorter Cu···C(N) distance of 2.293 Å and a smaller C–Pt–Cu angle of 55.8° in the boat conformation compared to the X-ray crystallographic data. Furthermore, the optimized P–Pt–Cu–P dihedral angles in both the boat and chair forms deviate from the X-ray data. Just like the case of [PtAu(μ-H$_2$PCH$_2$PH$_2$)$_2$(CN)$_2$]$^+$, the deviation of these optimized structural parameters from the X-ray crystallographic data is attributed to the floppy gas-phase model used in the calculation, which is different from the rigid crystal lattice. The shorter Cu–C(N) distance in the boat conformation reflects the presence of an intramolecular Cu–C(N) interaction. Previous work on dinuclear Cu(I) complexes[3g] revealed that the Cu(I)–solvent or Cu(I)–anion interactions would weaken the intramolecular Cu(I)···Cu(I) interactions, resulting in lengthening of this distance. Therefore, the shorter optimized Pt···Cu distance in the chair conformation relative to those in the boat conforma-
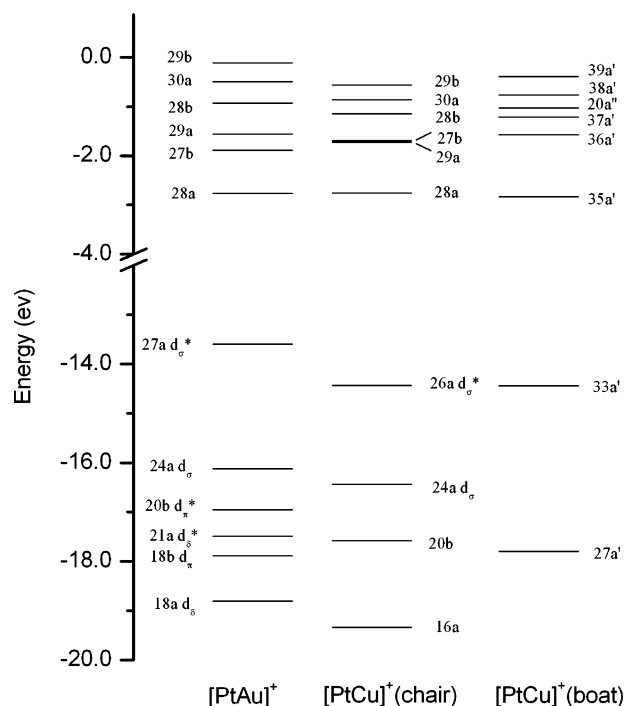
Figure 9. A simplified frontier MO diagram with large d(metal) compositions in $[PtM(\mu\text{-}H_2PCH_2PH_2)_2(CN)_2]^+$ (M = Au, Cu).

Table 3. Calculated Lower Energy Absorption Bands of the Model Complex at CIS Level with IPCM Method in CH_3CN and CH_2Cl_2

	λ_{calc} (nm)	oscillation strength	transition	λ_{obs} (nm)
$[PtAu(\mu\text{-}H_2PCH_2PH_2)_2(CN)_2]^+$				
in CH_3CN	290.9	0.0045	$X^1A{\rightarrow}A^1B$	
	259.78	0.5091	$X^1A{\rightarrow}B^1A$	316[a]
	246.47	0.1008	$X^1A{\rightarrow}C^1B$	259[a]
in CH_2Cl_2	289.23	0.0042	$X^1A{\rightarrow}A^1B$	
	259.13	0.5083	$X^1A{\rightarrow}B^1A$	317[a]
	246.18	0.1006	$X^1A{\rightarrow}C^1B$	265[a]
$[Pt_2(\mu\text{-}H_2PCH_2PH_2)_2(CN)_4]^b$	271.7	0.0029	$X^1A{\rightarrow}A^1A$	328[c]
$[Au_2(\mu\text{-}H_2PCH_2PH_2)_2]^{+}\cdot$ $(NCCH_3)_2{}^d$	245.7	0.284	$X^1A_g{\rightarrow}A^1A_u$	278/292

[a] From the absorption data of **4**. [b] See ref 39; calculation was undertaken at CIS level with the basis sets and geometry parameters being the same as those for $[Pt_2(\mu\text{-}H_2PCH_2PH_2)_2(CN)_4]$ in the ground state in ref 11. [c] From the absorption data of $[Pt_2(\mu\text{-dmpm})_2(CN)_4]$ in ref 11. [d] See ref 3k.

d_{z^2}, and 36.2% $d_{x^2-y^2}$ in MO 24a, 11.8% s, 16.9% d_{z^2}, and 11.1% $d_{x^2-y^2}$ in MO 27a). The total Pt/Au compositions in MO 24a and 27a are 25.4/55.7% and 42.9/42.2%, respectively. Therefore, it is difficult to explicitly label MOs 24a and 27a. Perhaps, they can be regarded as pseudo or distorted $d_\sigma/d_\sigma*$ orbitals, respectively.

For the $[PtCu(\mu\text{-}H_2PCH_2PH_2)_2(CN)_2]^+$ model, both the boat and chair conformations show that the d−d orbital overlapping is less significant than that found in the $[PtAu(\mu\text{-}H_2PCH_2PH_2)_2\text{-}(CN)_2]^+$ model. Only MOs 27a′ and 33a′ in the boat form and 16a, 20b, 24a, and 26a in the chair form have total metal compositions of >50% and >20% for Pt/Cu. However, the total metal compositions in these MOs in the chair form are ~10% higher than those in the boat form, which is consistent with the shorter Pt−Cu distance in the former. It is difficult to categorize these orbitals because of the low metal compositions. MOs 24a and 26a in the chair form can be regarded as the pseudo or distorted $d_\sigma/d_\sigma*$ type orbitals; they are due to a combination of s, d_{z^2}, $d_{x^2-y^2}$, and d_{xy}.

The pairs of MOs 18a/21a, 18b/20b, and 24a/27a in $[PtAu(\mu\text{-}H_2PCH_2PH_2)_2(CN)_2]^+$ and MOs 24a/26a in the chair form of $[PtCu(\mu\text{-}H_2PCH_2PH_2)_2(CN)_2]^+$ are pairs of d-bonding and -antibonding orbitals. The corresponding d orbital splittings are 1.22, 0.94, and 2.52 ev in $[PtAu(\mu\text{-}H_2PCH_2PH_2)_2(CN)_2]^+$ and 2.00 ev in $[PtCu(\mu\text{-}H_2PCH_2PH_2)_2(CN)_2]^+$, which are comparable to the corresponding values of 0.7−2.7 ev in $[Pt_2(\mu\text{-}H_2PCH_2PH_2)_2(CN)_4]$ (particularly the splitting of the MOs with d_{z^2} parentage of 2.66 ev).

As shown in Tables S5−S7, the LUMOs are either metal−metal and/or metal−P_{ligand} interactive orbitals. The contribution of metals is mainly from $(n + 1)$s, p orbitals.

Based on the optimized structure, the low-lying dipole-allowed electronic transitions in $[PtAu(\mu\text{-}H_2PCH_2PH_2)_2(CN)_2]^+$ in CH_3CN and CH_2Cl_2 were calculated by CI-singles method with the IPCM model and the results are listed in Table 3. The density diagrams of the frontier orbitals for the low-lying dipole-allowed electronic transitions of $[PtAu(\mu\text{-}H_2PCH_2PH_2)_2(CN)_2]^+$ in CH_3CN are depicted in Figure 10 (on simplification the similar case in the electrostatic field of CH_2Cl_2 is not shown).

The optimized molecular structures of *trans*-$[Pt(PH_3)_2(CN)_2]$, $[Au(PH_3)_2]^+$, and $[trans\text{-}Pt(PH_3)_2(CN)_2\text{-}Au(PH_3)_2^+]$ are listed in Table 4. The optimized C−Pt−Au angles are 90.7 and 87.8° in skewed and eclipsed geometry, respectively, which slightly deviate from 90.0°. However, the optimized P−Pt−Au and
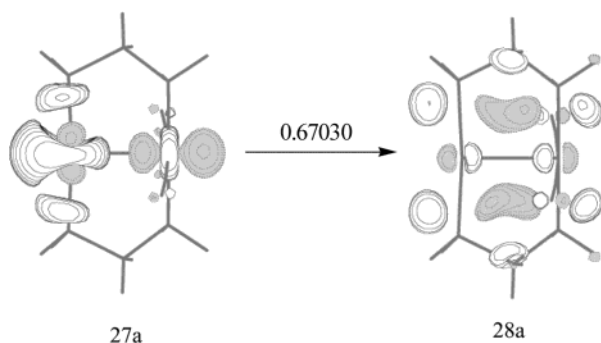
tion of $[PtCu(\mu\text{-}H_2PCH_2PH_2)_2(CN)_2]^+$ and **6** as determined by X-ray crystal analysis is attributed to Cu−C(N) interactions. The other calculated bonding parameters for $[PtCu(\mu\text{-}H_2PCH_2PH_2)_2(CN)_2]^+$ are consistent with the related structural data of **6**. A quantitative simplified MO diagram for the higher occupied (with nd contribution of metals) and lower unoccupied molecular orbitals for $[PtAu(\mu\text{-}H_2PCH_2PH_2)_2(CN)_2]^+$ and $[PtCu(\mu\text{-}H_2PCH_2PH_2)_2(CN)_2]^+$ is depicted in Figure 9. The partial MO compositions for these model compounds are summarized in Tables S5−S7 (see Supporting Information).

As shown in Tables S5−S7 and Figure 9, there are few frontier MOs arising from overlapping between the d orbitals of Pt and Au/Cu (which is important character for metal−metal bonding interaction) for the model compound, but most of the d orbitals undergo interaction with the ligands. This is different from the MOs of the $[Pt_2(\mu\text{-}H_2PCH_2PH_2)_2(CN)_4]$,[11] which were calculated at the same theoretical level. In $[Pt_2(\mu\text{-}H_2PCH_2PH_2)_2\text{-}(CN)_4]$, MOs 28a/33a have d_{z^2} composition of 78.1/66.0%, which are regarded as $d_\sigma/d_\sigma*$; MOs 22b/23b have d_{yz} compositions of 81.4/73.1%, and MOs 24b/28b have d_{xz} compositions of 87.0/78.1%, which are designated as $d_\pi/d_\pi*$ orbitals, respectively.

For $[PtAu(\mu\text{-}H_2PCH_2PH_2)_2(CN)_2]^+$, MOs 18a, 21a, 18b, 20b, 24a, and 27a have large metal compositions (totally > 50% and > 20% for Pt and Au, respectively). MOs 18a/21a are $d_\delta/d_\delta*$ orbitals, respectively, with substantial d_{xy} and/or $d_{x^2-y^2}$ parentage (23.1% d_{xy} + 4.5% d_{z^2} + 3.6% $d_{x^2-y^2}$ of Pt, 16.4% d_{xy} + 4.2% d_{z^2} of Au in MO 18a; 15.1% d_{xy} + 13.8% $d_{x^2-y^2}$ of Pt, 43.0% d_{xy} of Au in MO 21a). MOs 18b/20b are $d_\pi/d_\pi*$ orbitals, respectively, with d_{xz}(Pt, Au) of (29.7, 43.8%)/(28.9, 54.0%). The compositions of MOs 24a and 27a are complex, in which the main parentage of Pt orbitals is $5d_{z^2}$ (22.5% in MO 24a and 36.0% in MO 27a) with little 6s character (1.7% in MO 24a and 5.9% in MO 27a), while the contribution from Au is the hybrid of $5d_{z^2}$, $5d_{x^2-y^2}$, and 6s orbitals (14.5% s, 4.2%

Figure 10. Single electronic transition with |CI coefficients| > 0.1 in the CIS calculation for the dipole-allowed absorption at 259.78 nm of [PtAu-(μ-H$_2$PCH$_2$PH$_2$)$_2$(CN)$_2$)]$^+$ in CH$_3$CN.

Table 4. Partial Optimized Structural Parameters of *trans*-[Pt(PH$_3$)$_2$(CN)$_2$], [Au(PH$_3$)$_2$]$^+$, and the Dimer [*trans*-Pt(PH$_3$)$_2$(CN)$_2$–Au(PH$_3$)$_2$$^+$]

	trans-[Pt(PH$_3$)$_2$(CN)$_2$]	[Au(PH$_3$)$_2$]$^+$	skewed dimer	eclipsed dimer
Bond Length (Å)				
Pt···Au			2.950	2.904
Pt–P	2.378		2.330	2.326
Au–P		2.329	2.357	2.356
Pt–C	1.998		1.992	1.994
C–N	1.190		1.191	1.191
H–P(Pt)	1.416		1.416	1.416
H–P(Au)		1.415	1.415	1.416
Bond Angle (deg)				
H–P–Pt	115.6		116.1	116.4
H–P–Au		115.7	116.1	117.4
P–Pt–Au			93.3	98.0
P–Au–Pt			99.5	108.7
C–Pt–Au			90.7	87.8

P–Au–Pt angles of 93.3/98.0° and 99.5/108.7° in a skewed/eclipsed dimer, respectively, substantially deviate from 90.0°, indicating that the original planar [PtP$_2$C$_2$] and linear [AuP$_2$] units in the monomers change considerably upon formation of the dimer. Therefore, we use the optimized dimer structure to calculate the interaction energy. The other optimized structural parameters in the monomer and dimer are similar.

Discussion

Metal–Metal Distances. Intramolecular metal–metal distance is an important structural feature for assessing metal–metal interaction between closed shell metal ions. The intramolecular metal···metal distances of 2.9534(4), 2.9117(6), and 2.7368(4) in **4**, **5**, and **6**, respectively, are comparable to the corresponding values in a series of d⁸–d¹⁰ heteronuclear analogues (see Table 5), for instance, Pt···Au distances of 3.046-(2)/2.910(1) Å in [PtAu(μ-dppm)$_2$(CN)$_2$]ClO$_4$[6a] and [PtAu(μ-dppm)$_2$(C≡CPh)$_2$]PF$_6$·H$_2$O,[6c] Pt···Ag distances of 3.002(1)/3.146(3) Å in [PtAg(μ-dppm)$_2$(CN)$_2$(CF$_3$SO$_3$)][6b] and [PtAg(μ-dppm)$_2$(C≡CPh)$_2$I],[31] Ir···Au distances of 2.986(1)/2.944(1) Å in [IrAu(μ-dppm)$_2$(CO)Cl]PF$_6$[5a] and [IrAu(μ-dppm)$_2$(CNCH$_3$)$_2$]-PF$_6$,[5b] and Pt···Cu distances of 2.931(2)–3.021(2) Å in [Pt$_2$-Cu$_4$(C≡CPh)$_8$]$_2$.[32] The metal···metal distances in **4**–**6** are also comparable to those in homodinuclear d⁸ or d¹⁰ analogues (see Table 5), that is, the Pt···Pt, Au···Au, and Cu···Cu distances

Table 5. Metal···Metal Distances

complex	M···M (Å)	reference
[Pt$_2$(μ-dcpm)$_2$(CN)$_4$]	3.0565(4)	1l
[Pd$_2$(μ-dcpm)$_2$(CN)$_4$]	3.0432(7)	1m
[Ni$_2$(μ-dcpm)$_2$(CN)$_4$]	2.957(1)	1l
[Cu$_2$(μ-dcpm)$_2$](ClO$_4$)$_2$	2.685	3g
[Ag$_2$(μ-dcpm)$_2$](PF$_6$)$_2$	2.938(1)	3h
[Au$_2$(μ-dcpm)$_2$](ClO$_4$)$_2$	2.9389(9)	3j
[PtAu(μ-dcpm)$_2$(CN)$_2$]ClO$_4$ (**4**)	2.9534(4)	this work
[PtAg(μ-dcpm)$_2$(CN)$_2$]CF$_3$SO$_3$ (**5**)	2.9117(6)	this work
[PtCu(μ-dcpm)$_2$(CN)$_2$]BF$_4$ (**6**)	2.7368(4)	this work
[PdAu(μ-dcpm)$_2$(CN)$_2$]Cl (**7a**)	2.954(1)	this work
[NiAu(μ-dcpm)$_2$(CN)$_2$]ClO$_4$ (**8**)	2.8614(8)	this work
[PtAu(μ-dppm)$_2$(CN)$_2$]ClO$_4$	3.046(2)	6a
[IrAu(μ-dppm)$_2$(CO)Cl]PF$_6$	2.986(1)	5a
[IrAu(μ-dppm)$_2$(CNCH$_3$)$_2$](PF$_6$)$_2$	2.944(1)	5b
[PtAg(μ-dppm)$_2$(CN)$_2$(CF$_3$SO$_3$)]	3.002	6b
[Pt$_2$Cu$_4$(C≡CPh)$_8$]$_2$	2.931(2)–3.021(2)	32

of 3.0565(4), 2.9389(9), and 2.685 Å in [Pt$_2$(μ-dcpm)$_2$(CN)$_4$], [Au$_2$(μ-dcpm)$_2$](ClO$_4$)$_2$,[3j] and [Cu$_2$(μ-dcpm)$_2$](ClO$_4$)$_2$,[3g] respectively. We note that the Pt(II)···M(I) distances of 2.6–3.1 Å in **4**–**6** allow close metal–metal contacts and are reminiscent of weak metal–metal interactions. The relatively short metal–metal distance of 2.7368(4) Å in **6** could be due to the smaller ionic radii of Cu(I) compared to Au(I) or Ag(I) (0.96 for Cu(I), 1.26 for Ag(I), and 1.37 Å for Au(I)[33]). The Pd···Au distance of 2.954(1) Å in **7a** is nearly the same as the Pt···Au separation of 2.9534(4) Å in **4**. Therefore, the Pd–Au interaction in **7a** should be weaker than the Pt–Au interaction in **4** since the van der Waals radii[30] of the Pd atom is 0.1 Å shorter than that of the Pt atom. The Ni···Au distance of 2.8614(8) Å in **8** is shorter than the sum of van der Waals radii of 3.29 Å ("Ni + Au"), the metal···metal distances in dinuclear Pt(II), Pd(II), and Ni(II) analogues, and the metal···metal distances in the homodinuclear analogues of [Au$_2$(μ-dcpm)$_2$]$^+$ (2.9389(9) Å)[3j] and [Ni$_2$(μ-dcpm)$_2$(CN)$_4$] (2.957(1) Å).[1l]

Spectroscopic Properties. The absorption spectrum of **3** in CH$_2$Cl$_2$ (see Figure 2) is similar to that of *trans*-[Pt(P(*n*-Bu)$_3$)$_2$-(CN)$_2$] reported by Mason and co-workers[34] and *trans*-[Pt-(PCy$_3$)$_2$(CN)$_2$] (PCy$_3$ = tricyclohexylphosphine),[1l] in which cases intense absorptions were found at λ < 300 nm. According to previous work,[1l] these high-energy absorption bands are related to ^{1,3}{5d(Pt)→[6P$_z$(Pt), π*(C≡N), σ*(P–R)]} transitions. For the dinuclear complexes **4**–**6**, the absorption bands at 220–300 nm are comparable to that of **3** at a similar spectral region with small shifts in λ$_{max}$ and ϵ values; hence presumably these bands have a similar electronic origin. The salient feature in the absorption spectra of **4**–**6** is the intense absorption band at ca. 317, 306, and 331 (or 335) nm in **4**, **5**, and **6**, respectively, which is absent in the absorption spectra of **3**, [Au(PEt$_3$)$_2$]PF$_6$,[35] [Ag(PR$_3$)$_2$]ClO$_4$ (R = Me, Cy),[3h] and [Cu(PCy$_3$)$_2$]ClO$_4$.[3g] Such bands are comparable to related bands with λ$_{max}$ 323 (ϵ$_{max}$ 1.32 × 10⁴) and 317 nm (ϵ$_{max}$ 1.93 × 10⁴) in [PtAu(μ-dppm)$_2$-(CN)$_2$]ClO$_4$[6a] and [PtAg(μ-dppm)$_2$(CN)$_2$(CF$_3$SO$_3$)],[6b] respectively, which were previously assigned to ^{1}[nd$_{\sigma}$*→(n + 1)p$_{\sigma}$] transitions. We have made similar assignments accordingly. The weak absorption band at ca. 360 nm in **4** should be the spin-forbidden counterpart of the ^{1}(5d$_{\sigma}$*→6p$_{\sigma}$) transition. Here, the

(31) McDonald, W. S.; Pringle, P. G.; Shaw, B. L. *J. Chem. Soc., Chem. Commun.* **1982**, 861–864.

(32) Yam, V. W.-W.; Yu, K.-L.; Cheung, K.-K. *J. Chem. Soc., Dalton Trans.* **1999**, 2913–2915.

(33) *Handbook of Chemistry and Physics*; Weast: 1970–1971.

(34) Solar, J. M.; Ozkan, M. A.; Isci, H.; Mason, W. R. *Inorg. Chem.* **1984**, *23*, 758–764.

(35) Savas, M. M.; Mason, W. R. *Inorg. Chem.* **1987**, *26*, 301–307.

inferred singlet−triplet excited state splitting for **4** is 3998 cm^{-1}, which is comparable to the corresponding values of ~4000 cm^{-1} in [Pt$_2$(L)$_2$(CN)$_4$] (L = dcpm[11] or dppm[1f]) and 4259 cm^{-1} in [Pt$_2$(P$_2$O$_5$H$_2$)$_4$]$^{4-}$.[2] The proposed ^{1}(d$_\sigma$*→p$_\sigma$) transition bands in **4**−**6** are comparable in energy to related transitions in the homodinuclear d^8 and d^{10} complexes, such as [Pt$_2$(P$_2$O$_5$H$_2$)$_4$]$^{4-}$ (λ_{max} 367 nm, ϵ_{max} 45 400, in aqueous solution),[2] [Pt$_2$(μ-dcpm)$_2$-(CN)$_4$] (λ_{max} 337 nm, ϵ_{max} 24 100, in CH$_2$Cl$_2$),[11] [Au$_2$(μ-dcpm)$_2$]-(ClO$_4$)$_2$ (λ_{max} 278 nm, ϵ_{max} 28920, in CH$_3$CN),[3e] [Ag$_2$(μ-dcpm)$_2$](PF$_6$)$_2$ (λ_{max} 266 nm, ϵ_{max} 22000, in CH$_2$Cl$_2$),[3h] and [Cu$_2$(μ-dcpm)$_2$](ClO$_4$)$_2$ (λ_{max} 311 nm, ϵ_{max} 14090, in CH$_2$Cl$_2$; λ_{max} 319, ϵ_{max} 4820, in CH$_3$CN).[3g]

For **6** (see Figure 2 and inset), the intense absorption band at λ_{max} = 331 nm in CH$_3$CN/CH$_3$OH is slightly red-shifted to 335 nm in CH$_2$Cl$_2$, and there is also a significant difference in ϵ values in these solvents. A similar finding has also been observed for the 3d$_\sigma$*→4p$_\sigma$ transition in [Cu$_2$(μ-dcpm)$_2$]-(ClO$_4$)$_2$.[3g] This was attributed to coordination of CH$_3$CN molecules to Cu(I). Indeed, the crystal structure of [Cu$_2$(μ-dcpm)$_2$(CH$_3$CN)$_2$](ClO$_4$)$_2$[3g] with coordinated CH$_3$CN has been obtained. This kind of metal−solvent contact would weaken the intramolecular metal−metal interaction, leading to a reduced oscillation strength for the nd$_\sigma$*→(n + 1)p$_\sigma$ transition. In this work, a similar decrease in the extinction coefficient of the low-energy dipole-allowed transition of **6** upon changing the solvent from CH$_2$Cl$_2$ to CH$_3$CN was found. We have not been able to obtain crystals of **6** that show the existence of a weak PtCu···NCCH$_3$ interaction in the solid state. However, the chemical shift of the P atom ligated to Cu(I) in **6** in CD$_3$CN is shifted upfield by 3 ppm compared to that in CDCl$_3$ solution, suggesting interaction of CD$_3$CN with Cu(I). Similar findings derived from the ^{31}P chemical shifts have been described for [Cu$_2$(μ-dcpm)$_2$](ClO$_4$)$_2$.[3g]

The UV−vis absorption spectrum of **7** (see Figure 3) is different from those of **4**−**6** in that the higher energy absorption bands at λ < 298 nm have larger ϵ values ((1.7−2.2) × 10^4) than the lowest energy dipole-allowed ones at λ > 298 nm (n × 10^3), while, in the cases of **4**−**6**, the lowest energy dipole-allowed transitions are the most intense. The distinct absorption bands in CH$_2$Cl$_2$, CH$_3$CN, and CH$_3$OH at λ_{max} < 298 nm (ϵ (1.7−2.2) × 10^4) for **7** are proposed to originate from electronic transitions of the Pd(P)$_2$(CN)$_2$ unit, since the mononuclear [Pd(DEPE)$_2$](PF$_6$)$_2$ and *trans*-[Pd(P(n-Bu)$_3$)$_2$(CN)$_2$][34] derivatives display similar absorption bands. The shoulder absorption of **7** at 300−350 nm (ϵ = 5000−7000) is absent in related mononuclear Pd(II) complexes and [Au(PEt$_3$)$_2$]PF$_6$.[35] It is comparable to the shoulder absorption of [Pd$_2$(μ-dcpm)$_2$-(CN)$_4$][1m] at ca. 310 nm (ϵ = 4890) in solution. The 310 nm shoulder band of [Pd$_2$(μ-dcpm)$_2$(CN)$_4$] is blue-shifted with a decrease in temperature and has been assigned to the ^{1}(4d$_\sigma$*→5p$_\sigma$) transition, which is affected by solution temperature. We found that there is also a slight blue-shift of the above shoulder band of **7** from ca. 314 nm to ca. 300 nm upon decreasing the temperature from 298 to 203 K. Accordingly, we assign this shoulder absorption band of **7** to the ^{1}(d$_\sigma$*→p$_\sigma$) transition.

For **8**, the absorption bands between 300 and 500 nm are similar to those at λ_{max} (ϵ) 306 (5300), 361 (3700), and 391 nm (3900) for [Ni$_2$(μ-dcpm)$_2$(CN)$_4$][11] in CH$_2$Cl$_2$ solution. We have assigned the absorption bands of [Ni$_2$(μ-dcpm)$_2$(CN)$_4$] at 300−500 nm to d→d electronic transitions that involve marked

pyramidalization at the Ni atoms. Here, the Ni atom in **8** is also distorted from inversion site symmetry with C−Ni−C and P−Ni−P angles of 173.3(3)° and 172.95(6)°, respectively. Accordingly, we assign the absorption bands at 300−500 nm in **8** to d→d transitions. The intense absorption band at 277 nm (ϵ 26 500) for **8** is comparable to the bands at 251 nm (ϵ 55 400) for [Ni$_2$(μ-dcpm)$_2$(CN)$_4$] and 264 nm (ϵ 49 600) for *trans*-[Ni-(PCy$_3$)$_2$(CN)$_2$],[11] which are regarded as being associated with the Ni−P unit. The average Ni−P distance of 2.237 Å in **8** is shorter than that in *trans*-[Ni(PCy$_3$)$_2$(CN)$_2$] (2.243 Å), which is consistent with the corresponding decrease in transition energy. Accordingly, no Ni−Au interaction is depicted in the absorption spectrum of **8**.

Resonance Raman Spectra Analysis. Resonance Raman spectroscopy confirmed that the 317 and 335 nm absorption bands in **4** and **6**, respectively, are due to metal-centered nd$_\sigma$*→(n + 1)p$_\sigma$ transitions. The single low-frequency mode and their overtones are consistent with the Pt(II)−Au(I) and Pt(II)−Cu-(I) stretches. This reveals that the excited state distortion is localized in the Pt(II)−Au(I) or Pt(II)−Cu(I) bond. The assigned ν(PtAu) of 85 cm^{-1} and ν(PtCu) of 117 cm^{-1} are comparable to the ν(Pt$_2$) of 93 cm^{-1} for [Pt$_2$(μ-dcpm)$_2$(CN)$_4$],[11] ν(Au$_2$) of 88 cm^{-1} for [Au$_2$(μ-dcpm)$_2$]$^{2+}$,[3f] ν(Cu$_2$) of 104 cm^{-1} for [Cu$_2$-(μ-dcpm)$_2$]$^{2+}$,[3g] and ν(Rh$_2$) of 79 cm^{-1} for [Rh$_2$b$_4$]$^{2+}$ (b = 1,3-diisocyanopropane).[1a] Using a previously described method of calculation,[9] the excited state Pt−Au stretching vibration is estimated to be 128 cm^{-1} for **4**, which is larger than that in the ground state and in agreement with the assignment of the transition to an excited state with increased metal−metal bonding. This excited state M−M stretching frequency is similar to the corresponding frequencies of [Pt$_2$(μ-dcpm)$_2$(CN)$_4$] (145 cm^{-1}),[11] [Au$_2$(μ-dcpm)$_2$](ClO$_4$)$_2$ (175 cm^{-1}),[3f] [Cu$_2$(μ-dcpm)$_2$]-(ClO$_4$)$_2$ (150 cm^{-1}),[3g] and [Rh$_2$b$_4$]$^{2+}$ (144 cm^{-1})[1a] and also comparable with the value of 156 cm^{-1} for [Pt$_2$(P$_2$O$_5$H$_2$)$_4$]$^{4-}$,[36] which is regarded as having a single metal−metal bond in the excited state. However, a similar calculation method[9] estimated the Pt−Cu excited state stretching frequency for **6** to be 230 cm^{-1}, which is even higher than the excited Cu−Cu stretching frequency of 175 cm^{-1} for the related [Cu$_2$(μ-dcpm)$_2$](ClO$_4$)$_2$. The Pt···Au distance for **4** in the excited state calculated with the related method[9] is 0.10 Å shorter than that in the ground state. This M···M contraction upon excitation is comparable to those reported for [Pt$_2$(μ-dcpm)$_2$(CN)$_4$] (0.11 Å)[11] and [Au$_2$(μ-dcpm)$_2$](ClO$_4$)$_2$ (0.156 Å),[3f] but smaller than those for [Pt$_2$(P$_2$O$_5$H$_2$)$_4$]$^{4-}$ (0.225 Å from the resonance Raman spectroscopy[36] and 0.28(9) Å from the time-resolved X-ray crystallography[37]) and [Rh$_2$b$_4$]$^{2+}$ (~0.3 Å).[1b] We can see that changes in metal−metal distances in the excited states of the d^8−d,[8] d^{10}−d,[10] and d^8−d^{10} systems described previously and in this work are smaller than that for [Pt$_2$(P$_2$O$_5$H$_2$)$_4$]$^{4-}$. We suggest that the bridging phosphine ligand also exerts an effect on the metal−metal interaction.

Emission. The emissions of **4** and **5** are attributed to phosphorescence due to their long emission lifetimes (in microsecond regime) and large Stokes shifts (~9000 cm^{-1}) between the absorption and emission maxima. Excitation spectra

(36) Che, C.-M.; Butler, L. G.; Gray, H. B.; Crooks, R. M.; Woodruff, W. H. *J. Am. Chem. Soc.* **1983**, *105*, 5492−5494.
(37) Kim, C. D.; Pillet, S.; Wu, G.; Fullagar, W. K.; Coppens, P. *Acta Crystallogr. A* **2002**, *58*, 133−137.

measured in 77 K glassy solution (CH₃OH/EtOH 4:1) resemble the corresponding absorption spectra of **4** and **5** at room temperature.

Complex **7a** shows phosphorescence with emission maxima at 510–520 nm and lifetimes in the microsecond regime. The excitation spectrum measured in 77 K glassy solution is different from the absorption spectrum measured in CH₃OH at 298 K but resembles that recorded at 203 K, in which the broad absorption band at 300–350 nm at 298 K becomes a distinct shoulder and blue-shifts to ca. 290–315 nm, and a $^1[d_\sigma^* \rightarrow p_\sigma]$ transition is assigned. The emission of **7a** cannot be attributed to the triplet congener of the 290–315 nm transitions measured in CH₃OH at 203 K because of the large Stokes shift (~13 000 cm⁻¹). We propose that the emission originates from the $^3(d_\pi^* p_\sigma)$ or $^3(d_\delta^* p_\sigma)$ excited state, which lies at a lower energy.

The emission behavior of **6** is complex. This complex shows a long-lived emission (5–6 μs) with $\lambda_{max} = 508$ nm in solid state at 298 K, which is assigned to the phosphorescence of the $^3(d_\sigma^* p_\sigma)$ excited state. In solution at room temperature and in glassy solution at 77 K, the high-energy emission band at 430–460 nm with lifetimes in the microsecond regime resembles the $^3(d_\sigma^* p_\sigma)$ emission of **4** at 430–450 nm. The Stokes shifts of 6900–8300 cm⁻¹ for the singlet $d_\sigma^* \rightarrow p_\sigma$ transition are also comparable to that of **4** (~9000 cm⁻¹); we therefore assign the 430–460 nm emission of **6** to be $^3(d_\sigma^* p_\sigma)$ in nature. This assignment is confirmed by the excitation spectrum monitored at 445 nm in the glassy state, which resembles the absorption spectrum at 298 K. The low-energy emission at 490–590 nm recorded in solution at 298 K and in 77 K glassy solution (CH₃-OH/EtOH 4:1) has a different excitation spectrum (monitored at 493 nm in 77 K glassy solution) from the absorption spectrum measured in solution at room temperature. The broad emission band indicates significant distortion in the excited state. As in the case of $[Cu_2(\mu\text{-dcpm})_2]^{2+}$,[38] we suggest that coordination of solvent/anions (S) to give $[PtCu(\mu\text{-dcpm})_2(CN)_2(S)_n]^+$, which is present in low concentration, could be responsible for the 490–590 nm emission.

Calculated Electronic Transitions. The $[PtAu(\mu\text{-}H_2PCH_2PH_2)(CN)_2]^+$ molecule has a ^1A ground state. As shown in Table 3, the calculated low-lying dipole-allowed transitions with the IPCM model in CH₃CN and CH₂Cl₂ solutions are virtually identical. This is consistent with the finding that the absorption spectra of **4** in these two solvents are almost the same. The calculated dipole-allowed $X^1A \rightarrow B^1A$ transition at 259.78 nm in CH₃CN and 259.13 nm in CH₂Cl₂ has a larger oscillator strength (0.5091 and 0.5083, respectively) than the lower energy $X^1A \rightarrow A^1B$ transition at 290.90 and 289.23 nm (oscillator strength 0.0045 and 0.0042). Therefore, we suggest that the former should be correlated to the intense absorption band of **4** at $\lambda_{max} = 317$ nm in solution.

The $X^1A \rightarrow A^1B$ transition calculated at 290 nm is mainly composed of the following transitions: MO 26b → MO 28a, MO 26b → MO 29a, with |CI coefficients| of 0.653 28 and 0.156 25, respectively (see Figure S7). However, due to the weak oscillator strength (~0.004), we propose that this transition is unlikely to be detected under normal experimental conditions or would be masked by the tail of the intense $X^1A \rightarrow B^1A$ transition.
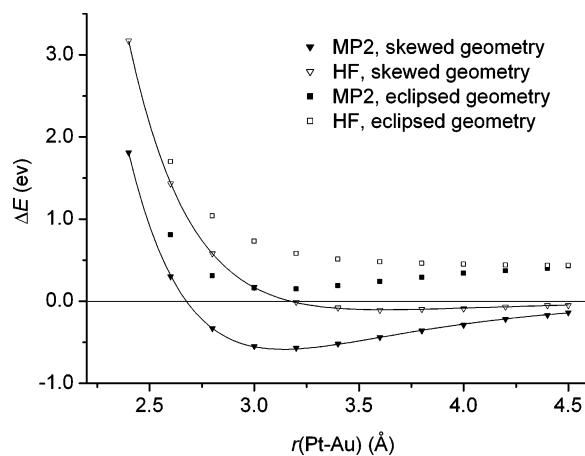
(38) Mao, Z.; Chao, H.-Y.; Hui, Z.; Che, C.-M.; Fu, W.-F.; Cheung, K.-K.; Zhu, N. *Chem.—Eur. J.* **2003**, *9*, 2885.

Figure 11. Interaction energy curve of $[trans\text{-}Pt(PH_3)_2(CN)_2\text{-}Au(PH_3)_2^+]$ calculated by Counterpoise method.

The $X^1A \rightarrow B^1A$ transition calculated at 259 nm (see Figure 10) is mainly due to the transition of MO 27a → MO 28a with |CI coefficients| of 0.670 30. As discussed above, MO 27a is a d_σ^* type orbital. MO 28a is the combination of p_z(metal) and ψ(P$_{ligand}$) and can be described as [p$_\sigma$(metal) + ψ(P$_{ligand}$)]. Therefore, the $X^1A \rightarrow B^1A$ transition has $^1[d_\sigma^* \rightarrow p_\sigma]$ character though the metal-to-ligand charge-transfer parentage could not be neglected.

The $X^1A \rightarrow C^1B$ transition (see Figure S8) mainly involves the transition of MO 27a → MO 27b with |CI coefficients| of 0.655 42. MO 27b is an Au–P π-type interaction orbital. This transition should be related to the higher energy absorptions of **4** at $\lambda < 300$ nm.

From the above analysis, we can see that the calculated lower energy intense absorption band at 259 nm ($X^1A \rightarrow B^1A$) contains some MLCT character and is not a pure metal centered $d_\sigma^* \rightarrow p_\sigma$ electronic transition. This is different from the case of the d^{10}–d^{10} system $[Au_2(H_2PCH_2PH_2)]^{2+}$,[3k] in which the calculated absorption band at 245.7 nm is mainly a $^1[d_\sigma^* \rightarrow p_\sigma]$ transition combined with a $^1[d_\sigma^* \rightarrow s_\sigma]$ transition at a ratio of 5:1. For the d^8–d^8 system $[Pt_2(\mu\text{-}H_2PCH_2PH_2)(CN)_4]$, the calculated low-lying dipole-allowed absorption band at 271.69 nm is characterized as a $^1[d_\sigma^* \rightarrow (sp)_\sigma + d_\delta]$ electronic transition.[39] Therefore, the excited states for the d^8–d,⁸ d^{10}–d,¹⁰ and d^8–d^{10} dinuclear systems are somewhat different. We propose that this is due to the different electronic configurations of the metal atoms in these systems. The high-lying occupied MOs in all these systems are d_σ^* (d_{z^2}–d_{z^2}) since the d_σ/d_σ^* orbitals have the largest splitting compared to other d–d interaction orbitals. However, the low-lying unoccupied MOs can be different since the d^8 metal atom has an empty $5d_{x^2-y^2}$ orbital but the 5d orbitals of the d^{10} metal atom are fully occupied.

For the $X^1A \rightarrow B^1A$ transition of $[PtAu(\mu\text{-}H_2PCH_2PH_2)(CN)_2]^+$, the terminated orbital 28a is a metal–metal bonding-type orbital. Therefore, the metal–metal bond order would increase upon electronic transition. This is consistent with the resonance Raman results showing that the metal–metal stretching frequency of **4** is enhanced in the excited state.

[Pt(II)–Au(I)] Interaction Energy in Ground State. As depicted in Figure 11, the interaction energy curves of the $[trans\text{-}Pt(PH_3)_2(CN)_2\text{-}Au(PH_3)_2^+]$ dimer are attractive for the skewed

(39) Xia, B.-H. Ph.D. Thesis, The University of Hong Kong, 2002.

geometry but repulsive for the eclipsed geometry at both HF and MP2 levels. Hence, Pt(II)−Au(I) interaction exists in the ground state with the skewed geometry, and no interaction has been found for the eclipsed geometry. The attractive effect at the HF level signifies weak bonding interaction due to orbital overlap between the two metal centers.

The well depth for the skewed structure is −0.59 ev (−13.6 kcal mol^{-1}) at r(Pt−Au) = 3.14 Å at the MP2 level and −0.1 ev (−2.3 kcal mol^{-1}) at r(Pt−Au) = 3.62 Å at the HF level. These values cannot be regarded as the real Pt(II)−Au(I) interaction energy because the interaction energy curve is shallow and does not reach the zero point even at r(Pt−Au) = 4.5 Å (ΔE = −0.14 and −0.05 ev at MP2 and HF level, respectively). If we assume that metal−metal bonding interaction vanishes at r(Pt−Au) = 4.5 Å, the attractive property of the ΔE value at r(Pt−Au) ≥ 4.5 Å should not arise from the metal−metal *bonding* interaction and could be attributed to the long-range dispersion energy. Therefore, the well depth is corrected by the ΔE values at r(Pt−Au) = 4.5 Å. The corrected well depth is 0.45 ev (10.4 kcal mol^{-1}) at MP2 level and 0.05 ev at HF level; the latter value is sufficiently small to neglect, and the former can be compared with the well-documented Au(I)−Au(I) interaction energy of 5−10 kcal mol^{-1} [40] and the calculated d^8−d^8 metal−metal bonding energies of 9−20 kcal mol^{-1} in [PtCl$_2$(CO)$_2$]$_2$ and [PtCl$_2${HNCH(OH)}$_2$]$_2$.[41]

The calculated equilibrium Pt···Au distance r_{eq}(Pt−Au) of 3.14 Å at the MP2 level is longer than the Pt···Au separation of 2.9534(4) and 3.034(1) Å in **4** and [PtAu(μ-dppm)$_2$(CN)$_2$]-ClO$_4$, respectively. We should note that in **4** and [PtAu-(μ-dppm)$_2$(CN)$_2$]ClO$_4$ the two metal atoms are bridged by two phosphine ligands while the [*trans*-Pt(PH$_3$)$_2$(CN)$_2$−Au(PH$_3$)$_2$$^+$] consists of two unbridged subsystems *trans*-Pt(PH$_3$)$_2$(CN)$_2$ and Au(PH$_3$)$_2$$^+$. The bridging diphosphine ligands will shorten the metal−metal distance. The calculated equilibrium Pt···Au distance r_{eq}(Pt−Au) is also longer than the optimized Pt···Au distance of 2.9502 Å in the skewed [*trans*-Pt(PH$_3$)$_2$(CN)$_2$−Au-(PH$_3$)$_2$$^+$] dimer. In fact, the interaction energy curve does not describe the absolute minimum on the interaction energy surface for the [*trans*-Pt(PH$_3$)$_2$(CN)$_2$−Au(PH$_3$)$_2$$^+$] dimer since only one coordinate, r(Pt−Au), was varied during calculation. Therefore, the r_{eq}(Pt−Au) value obtained from the interaction energy curve

is not the real equilibrium Pt−Au distance of the dimer. Nevertheless, the r_{eq}(Pt−Au) of 3.14 Å is shorter than the sum of the van der Waals radii of "Pt + Au" (3.41 Å)[30] and within the range of separations expected for weak metal−metal interaction. These results strongly indicate the existence of weak Pt(II)−Au(I) interaction.

Concluding Remarks

The UV−vis spectroscopic properties of a series of d^8−d^{10} complexes have been examined in order to scrutinize the metal−metal interaction. Resonance Raman spectra of **4** and **6** indicate that the lowest energy dipole-allowed electronic transition is nd$_\sigma$*→(n + 1)p$_\sigma$ in nature and there is contracted metal−metal separation in the excited state. Theoretical calculations revealed that the electronic origin of d^8−d^{10} metal−metal interaction is complicated compared with d^8−d^8 or d^{10}−d^{10} systems. The calculation on the CIS level reveals that the lower energy dipole-allowed X^{1}A→B^{1}A electronic transition in [PtAu(μ-H$_2$PCH$_2$-PH$_2$)$_2$(CN)$_2$]$^+$ is different from the cases of [Pt$_2$(H$_2$PCH$_2$PH$_2$)$_2$-(CN)$_4$] and [Au$_2$(H$_2$PCH$_2$PH$_2$)$_2$]$^{2+}$ and is ^{1}[d$_\sigma$*→p$_\sigma$] in nature mixed with MLCT character. The attractive nature of the interaction energy curve for the [*trans*-Pt(PH$_3$)$_2$(CN)$_2$−Au-(PH$_3$)$_2$$^+$] dimer confirms the weak Pt(II)−Au(I) interaction in the ground state.

Supporting Information Available: Crystal data for **4**·2CH$_3$-OH, **5**·CH$_3$OH, **6**·CH$_2$Cl$_2$, **7a**·0.5C$_2$H$_5$OC$_2$H$_5$·1.5H$_2$O, and **8**·2CH$_3$OH (Table S1), selected bond distances and bond angles for **4**−**8** (Table S2), resonance Raman data of **4** and **6** in CH$_2$-Cl$_2$ (Tables S3 and S4), partial MO compositions of [PtAu(μ-H$_2$PCH$_2$PH$_2$)$_2$(CN)$_2$] and [PtCu(μ-H$_2$PCH$_2$PH$_2$)$_2$(CN)$_2$] (Tables S5−S7), perspective drawings of **5**−**8** (Figures S1−S4), emission spectra of **5** (Figure S5), resonance Raman spectra of **6** in CH$_2$Cl$_2$ (Figure S6), single electronic transitions with |CI coefficients| > 0.1 in the CIS calculation for the 290.9 and 246.5 nm absorptions of [PtAu(μ-H$_2$PCH$_2$PH$_2$)$_2$(CN)$_2$]$^+$ in CH$_3$CN (Figures S7 and S8), and the CIF files for all the crystal structures reported in this paper. This material is available free of charge via the Internet at http://pubs.acs.org.

JA0355325

(40) Schmidbaur, H. *Chem. Soc. Rev.* **1995**, *24*, 391−400.
(41) Novoa, J. J.; Aullón, G.; Alemany, P.; Alvarez, S. *J. Am. Chem. Soc.* **1995**, *117*, 7169−7171.